

1       **Surface area and  $\Omega$ -aragonite oversaturation as controls of the**  
2       **runaway precipitation process in ocean alkalinity enhancement**

3  
4       **Niels Suitner<sup>1</sup>, Jens Hartmann<sup>1</sup>, Selene Varliero<sup>2</sup>, Giulia Faucher<sup>3</sup>, Philipp Suessle<sup>3</sup>, and Charly A. Moras<sup>1</sup>**

5  
6       <sup>1</sup>Institute for Geology, University of Hamburg, Bundesstrasse 55, 20146 Hamburg, Germany

7       <sup>2</sup>Department of Chemistry, Materials and Chemical Engineering “Giulio Natta”, Politecnico di Milano,  
8       Milan; Italy

9       <sup>3</sup>GEOMAR Helmholtz Centre for Ocean Research Kiel, Wischhofstrasse 1-3, 24148 Kiel, Germany

10  
11       Correspondence: Niels Suitner     (niels.suitner@uni-hamburg.de),

12    Jens Hartmann   (geo@hattes.de)

13  
14       **Orcid:**

15       Niels Suitner:                    <https://orcid.org/0000-0003-3413-857X>

16       Jens Hartmann:                    <https://orcid.org/0000-0003-1878-9321>

17       Selene Varliero:                   <https://orcid.org/0000-0001-9532-2202>

18       Giulia Faucher:                    <https://orcid.org/0000-0001-8930-477X>

19       Philipp Suessle:                   <https://orcid.org/0000-0001-7224-2330>

20       Charly A. Moras:                   <https://orcid.org/0000-0001-6819-6167>

21 **Abstract**

22 Ocean alkalinity enhancement (OAE) is a strategy for marine carbon dioxide removal that aims to increase the  
23 total alkalinity (TA) of seawater to sequester atmospheric CO<sub>2</sub> in the form of dissolved inorganic carbon (DIC). An  
24 intense alkalization of seawater resulting from OAE treatment could trigger a significant runaway carbonate  
25 precipitation process, which may lead to a loss of initially added TAalkalinity, thereby limiting its efficiency. Even  
26 under natural background aragonite saturation states, a continuous yet barely detectable loss of TAalkalinity is  
27 theoretically expected to occur in seawater. With the additional increase through OAE, time ranges to initiate an  
28 appreciable TA-loss process could be reduced significantly. Therefore, predicting the TAalkalinity stability ranges  
29 might be a necessity for application scenarios. The main drivers of the precipitation process are i) the aragonite  
30 saturation state of seawater and ii) the available surface area for heterogeneous precipitation.

31 In this study, we refined the use of logistic functions to describe the temporal evolution of both drivers, with  
32 experimental datasets using natural seawater from the Raunefjorden (Bergen, Norway; Temp.: ~11°C, Sal.:  
33 ~32.6). The observed patterns were then used to derive a process-based model for calculating TA-loss rates,  
34 focusing on the accelerated precipitation phase of the runaway process while considering saturation levels and  
35 available particle surface area. The formation of carbonate phases reduces seawater TA concentrations, inducing  
36 a delay or stopping the TA-loss process. In addition, the sinking of precipitated particles decreases the potential  
37 for further precipitation by reducing the available surface area in the system. To assess the impact of particle  
38 sinking on TA-loss, their shape and size distribution were determined. Under the environmental conditions  
39 presented here, TA-loss rates could be reduced by up to 30-40% due to the sinking of particles, after just one  
40 day.

41 Integrating the proposed concepts into ocean models could enhance the accuracy of predictions regarding the  
42 fate of added TAalkalinity. Gaining insights into the evolution of the identified, seemingly stable TA levels can  
43 help prevent accelerated precipitation phases. Additionally, an understanding of particle sinking or dilution  
44 processes reducing the available reactive particle surface area is relevant to assess the efficacy and durability of  
45 OAE.

46

## 47 1 Introduction

48 To mitigate climate change and reach net-zero greenhouse gas emissions by the end of the century, negative  
49 emission technologies (NETs) are necessary [besides greenhouse gas emission reduction](#) (UNFCCC, 2015)  
50 considering the slow change in the development of the energy infrastructure, lifestyle of humanity, and national  
51 goals for economic growth (Fuss et al., 2018; Iyer et al., 2015; Sers & Victor, 2018). Various carbon dioxide  
52 removal (CDR) technologies have been proposed to help achieve the necessary negative emission trajectories  
53 (Hartmann et al., 2013; IPCC, 2023; Minx et al., 2018; Rogelj et al., 2018). Among these, ocean alkalinity  
54 enhancement (OAE) is a promising CDR method (Harvey, 2008; Ilyina et al., 2013; Khesghi, 1995; Rau & Caldeira,  
55 1999), with the potential to geochemically sequester 3-30 Gt CO<sub>2</sub> yr<sup>-1</sup> (Oschlies et al., 2023; Renforth &  
56 Henderson, 2017).

57 [Enhancing total alkalinity \(TA\) Alkalinity enhancement](#) could be achieved by two addition approaches: **1.** a non-  
58 CO<sub>2</sub>-equilibrated (neq) or **2.** a CO<sub>2</sub>-equilibrated (eq) (Schulz et al., 2023). Through the neq approach, alkaline  
59 materials, such as silicate or hydroxide-based mineral phases could be introduced to seawater in the form of  
60 solids or solutions, allowing longer-term CO<sub>2</sub> equilibration with the atmosphere through ingassing of atmospheric  
61 CO<sub>2</sub>. In the eq approach, already partially pre-CO<sub>2</sub>-equilibrated solutions or carbonate-based substances could  
62 be released into seawater. Neq [TAalkalinity](#) addition strategies induce greater variations in the affected  
63 carbonate system, resulting in drastically reduced pCO<sub>2</sub> and a rapid increase in pH values. While an eq  
64 [TAalkalinity](#) addition results in less severe changes in ocean chemistry, it is less efficient in generating carbon  
65 sequestration potential (Schulz et al., 2023; Suitner et al., 2024).

66 Depending on the introduced alkalinization method (see Eisaman et al., 2023) and the magnitude of treatment,  
67 induced changes in the carbonate system could lead to adverse effects on biota (Faucher et al., 2024; Ferderer  
68 et al., 2022; Gately et al., 2023; Goldenberg et al., 2024; Marín-Samper et al., 2024; Sánchez et al., 2024; Xin et  
69 al., 2024) or in case of persistent oversaturation, result in the precipitation of secondary mineral phases and  
70 therefore a loss of the introduced [TAtotal alkalinity \(TA\)](#) (Ilyina et al., 2013; Schulz et al., 2023). The process of  
71 TA leakage as a consequence of OAE was recently described by several studies (see Fuhr et al., 2022; Hartmann  
72 et al., 2023; Moras et al., 2022; Pan et al., 2021; Ringham et al., 2024; Suitner et al., 2024; Varliero et al., 2024).  
73 Within these laboratory-based studies, self-sustaining runaway carbonate precipitation processes led to a  
74 significant decrease in the added [TAalkalinity](#), which could even result in a net-loss of TA. TA stability ranges, and  
75 the evolution of the precipitation process depend on the specific local environmental conditions such as  
76 temperature, salinity, aragonite saturation state ( $\Omega_{ar}$ ), or suspended particle load of the treated water mass  
77 (Moras et al., 2024).

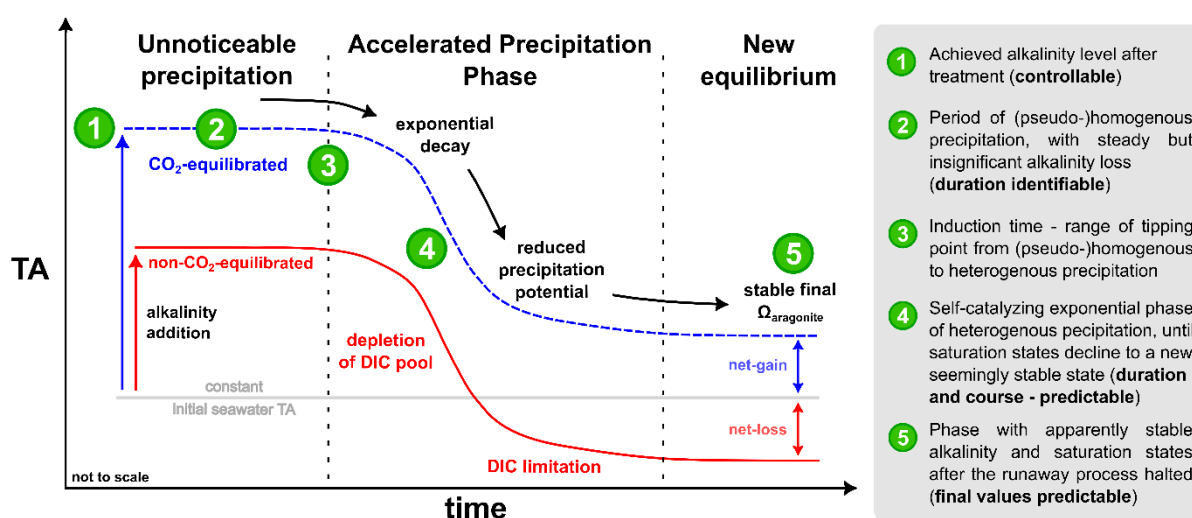
78 The objective of this study is to demonstrate the general capability to predict and parametrize the temporal  
79 evolution of a triggered runaway carbonate precipitation process during OAE approaches, based on quantifiable  
80 and measurable parameters. Estimations of stability ranges for the permanence of introduced [TAalkalinity](#)  
81 additions were derived from these parametrizations. The ability to predict TA stability ranges can help prevent  
82 secondary mineral formation and optimize assessments for future OAE application scenarios.

83 Suitner et al. (2024) demonstrated the potential of utilizing inverse logistic functions to depict the temporal  
 84 evolution of the TA-loss process during the runaway carbonate formation phase (see Fig. 1). In this study,  
 85 principal descriptive parameters such as TA addition and stability ranges to trigger the runaway process or the  
 86 timespan of the precipitation phase could be formalized based on their experimental dataset. This approach also  
 87 offers the possibility of a straightforward integration of time-dependent loss terms into predictive computational  
 88 models simulating OAE addition scenarios, as presented by He & Tyka (2023), Ou et al. (2025), Schwinger et al.  
 89 (2024) or Zhou et al. (2024).

90 The application of OAE may exceed critical levels for carbonate precipitation. For open ocean scenarios the rapid  
 91 initiation of mixing processes would efficiently reduce the potential for secondary carbonate formation.  
 92 Nevertheless, runaway carbonate formation may occur within enclosed geographic locations with physical  
 93 features such as bays, estuaries, or lagoons. In addition, thermohaline layering (Bialik et al., 2022) or high  
 94 sediment load (Wurgaft et al., 2016, 2021) might create conditions that lead to **TA-alkalinity** loss processes.

95 To sustain ~~a triggered~~the ~~observed~~ runaway carbonate formation (Fig. 1), it is ~~necessary~~essential to retain the  
 96 precipitates in the system. Removal of these particles reduces the potential for continuous heterogeneous  
 97 precipitation, thereby slowing down or halting the process. In this study, the empirically determined **TA-alkalinity**  
 98 loss rates were used to derive the quantity of precipitated particles. By identifying the particle sizes, shapes,  
 99 densities, and sinking velocities, their potential residence times in the water column were estimated.  
 100 Furthermore, we evaluated whether the formation of secondary minerals can supply sufficient surface area for  
 101 a continuous detectable heterogeneous runaway process in an open-water body and whether the process would  
 102 be interrupted or attenuated by removing particles due to their descent into deeper layers.

103



104

## 105 2 Material and methods

### 106 2.1 Overview of experimental setups

107 Three incubation experiments were conducted to examine the stability of TAalkalinity of the local “filtered”  
108 (mesh size 0.2  $\mu\text{m}$ ) and “unfiltered” (mesh size 50  $\mu\text{m}$ ) seawater of the Raunefjorden, Norway (60.27° N, 5.20°  
109 E). Within TA-gradient approaches, 250 ml polystyrene cell culture bottles were filled with natural seawater and  
110 incubated in a flow-through incubation box, following the natural light and temperature conditions.  
111 Runawayrunaway precipitation was observed in eq and neq treatments, after surpassing specific time and  
112 TAalkalinity addition ranges, allowing the description of patterns during the precipitation process. A detailed  
113 description of the experimental results, design and methods is already given in Suitner et al. (2024), a brief  
114 overview is also provided in Tab. 1 (also see SI for further details).  
115

Table 1: Overview of the experimental design of precipitation experiments, in Suitner et al. (2024)

| #   | filter mesh size  | CO <sub>2</sub> state to atmosphere | Alkaline material                                       | Runtime [days] | Range TA <sub>added</sub> [ $\mu\text{mol kg}^{-1}$ ] | TA <sub>added</sub> gradient steps [ $\mu\text{mol kg}^{-1}$ ] | Temperature [°C] |
|-----|-------------------|-------------------------------------|---|----------------|---|--|------------------|
| I   | 50 $\mu\text{m}$  | non-equilibrated (neq)              | NaOH  | 25             | 0-2800  | 200  | 10-11            |
| II  | 0.2 $\mu\text{m}$ |                                     |   |                | 0-3400  |  | 11-13            |
| III | 0.2 $\mu\text{m}$ | air-equilibrated (eq)               | Na <sub>2</sub> CO <sub>3</sub> /<br>NaHCO <sub>3</sub> | 20             | 0-9200  | 800  | 12-16            |

116

### 117 2.2 Curve fitting of the TA and $\Omega_{\text{ar}}$ evolution

118 The numerical curve fit model to describe the temporal development of TA and  $\Omega_{\text{ar}}$ , as presented in Suitner et al.  
119 (2024), was refined by additionally including the observed TA-loss rates as a second input factor, to provide  
120 continuous functions as a basis for further model calculations. The curve fit model utilized the consistent  
121 tendency of all observed runaway precipitation processes to follow inverse logistic trends in form of:

$$122 \quad f(t) = a e^{-b e^{-ct}} + d \quad (1)$$

123 for the temporal evolution of TA and  $\Omega_{\text{ar}}$ . The coefficients **(d)** and **(a)** are defined by the achieved level of TA/ $\Omega_{\text{ar}}$   
124 after the addition **(d)** and the final reached value after the runaway process halted **(a)**. Since these factors are  
125 predefined by the experimental setup, the curve fit model only numerically parameterizes the two coefficients  
126 **(b)** and **(c)**. Coefficient **(b)** represents the “induction time”, or the time required for CaCO<sub>3</sub> precipitation to  
127 become detectable in the TA measurements, depicted by the horizontal translation along the x-axis, while **(c)**  
128 denotes the timespan between start and end of an accelerated precipitation phase (APP). See Fig. 2 for a visual  
129 impression of the influence of iterations of each coefficient.

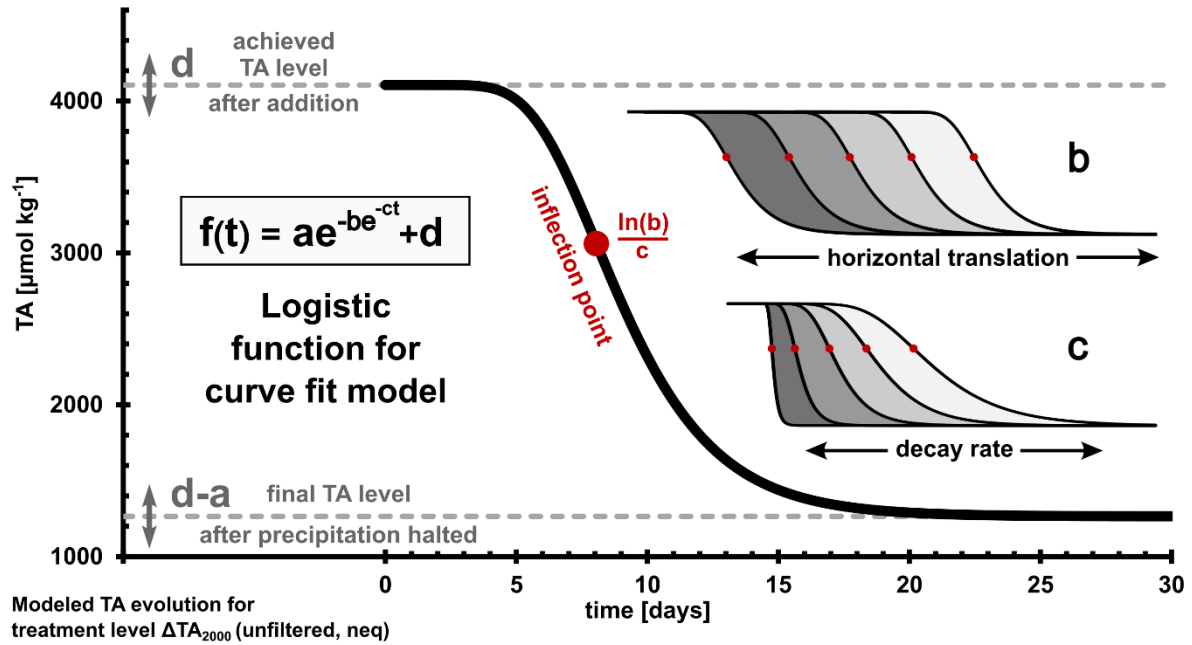


Figure 2: Overview and iterations of each coefficient (a)-(d) of the applied inverse logistic function for the numerical curve fitting; the inflection point is defined by  $\ln(b)/c$ ; for further characteristics see Tjørve & Tjørve (2017) [↗](#)

130

### 131 2.3 Empirical rate law and determination of loss rates

132 A simple empirical rate law was used to evaluate the precipitation rates  $R$  [ $\mu\text{mol m}^{-2} \text{h}^{-1}$ ] (see e.g. Inskeep &  
133 Bloom, 1985; Morse et al., 2007; Zhong & Mucci, 1989):

$$134 \quad R = k(\Omega_{ar} - 1)^n \quad (2)$$

135 The experimental TA-loss rates were then fitted to the logarithmic form of Eq. (2) to determine the coefficients  
136  $k$  (rate constant) and  $n$  (empirical reaction order):

$$137 \quad \log(R) = n(\Omega_{ar} - 1) + \log(k) \quad (3)$$

138 To correct for the variable surface area,  $r$  [ $\mu\text{mol h}^{-1}$ ] was normalized for the assumed available active mineral  
139 surface area ( $A$  in [ $\text{m}^2$ ]) (adapted from Sjöberg, 1976).

$$140 \quad r = k A (\Omega_{ar} - 1)^n \quad (4)$$

141 As the gradient approaches could not provide a sufficient amount of precipitates to determine their surface area,  
142 a one-week side experiment was conducted to estimate the mineral surface area generated during the runaway  
143 precipitation process. By adding 3.8 mmol NaOH and 7.0 mmol  $\text{NaHCO}_3$  to 40 L of 0.2  $\mu\text{m}$  filtered natural  
144 seawater (salinity 33) at 23°C, around 5 g of aragonite precipitates were generated to provide material for a BET  
145 surface area measurement. Using  $\text{N}_2$  adsorption (Brunauer et al., 1938), with a Quantachrome autosorb iQ at the  
146 University of Hamburg, a surface area of  $2.283 \pm 0.018 \text{ m}^2 \text{ g}^{-1}$  was determined. By the assumption that the surface  
147 area is constant for all precipitates and that the entire lost TA is transformed into aragonite particles, the  
148 experimentally determined TA-loss was used to calculate the surface area after each timestep, therefore allowing  
149 to correct the precipitation rates.

150

## 151 2.4 Particle analysis

152 The precipitated particles of three filters (0.2 $\mu$ m PC), collected during incubation experiments within previous  
153 campaigns published in Hartmann et al. (2023) (neq  $\Delta$ TA<sub>2400</sub>, Gran Canaria) and Suitner et al. (2024) (neq  $\Delta$ TA<sub>2600</sub>  
154 and  $\Delta$ TA<sub>2800</sub>, Raunefjorden, also see section 2.1). Similar to the incubations from the Raunefjorden, the filters  
155 from the Gran Canaria campaign originate from TA-gradient experiment, utilizing the local oligotrophic seawater  
156 (TA<sub>initial</sub>  $\sim$ 2411  $\mu$ mol kg<sup>-1</sup>, S  $\sim$ 36.6, pH  $\sim$ 8.15, T  $\sim$ 23 °C) to test the stability of alkalization approaches (see SI for  
157 further details). The filtered precipitates, were analyzed by scanning electron microscopy (SEM; Tabletop  
158 Microscope Hitachi TM4000plus - University of Hamburg) to determine shape, size and quantity of the  
159 precipitated material. Length, width and shape of each particle were specified by manual examination.  
160 If sufficient precipitated materials could be provided, the remaining SEM filter material was used to determine  
161 their sinking velocities, utilizing a FlowCam (Fluid Imaging Technologies Inc., Scarborough, United States). A  
162 detailed description of the setup is provided in Suessle et al. (2023) and references therein.

163 **3 Results**

164 **3.1 Numerical logistic curve-fittings**

165 Three OAE gradient approaches by Suitner et al. (2024) were examined to test the stability of TAalkalinity and to  
166 generate refined numerical logistic curve fittings of the temporal development of TA and  $\Omega_{ar}$  (Figs. 3, S1S2 and  
167 S2S3). The coefficients **(b)** and **(c)** (see Fig. 2) were determined by numerical interpolation to optimize the fit to  
168 Eq. (1) and its derivative in equal proportions. Therefore, the shown functions were optimized to describe the  
169 temporal evolution, while also including the rate loss changes, which allowed an improved description of the  
170 runaway process in comparison to the approaches in previous studies.Suitner et al. (2024). Outlying data points  
171 displaying an anomalous increase or stagnation in values in the filtered approaches were removed from curve-  
172 fitting calculations (for details see SI in Suitner et al., 2024). For each treatment, continuous differentiable  
173 functions to describe and analyze the runaway carbonate precipitation process during OAE approaches were  
174 generated. To illustrate the described processes and trends, the unfiltered neq approach was selected as an  
175 example (Fig. 3). The plots for the filtered approaches are provided in the SI (Figs. S1, S2 and S3).

176

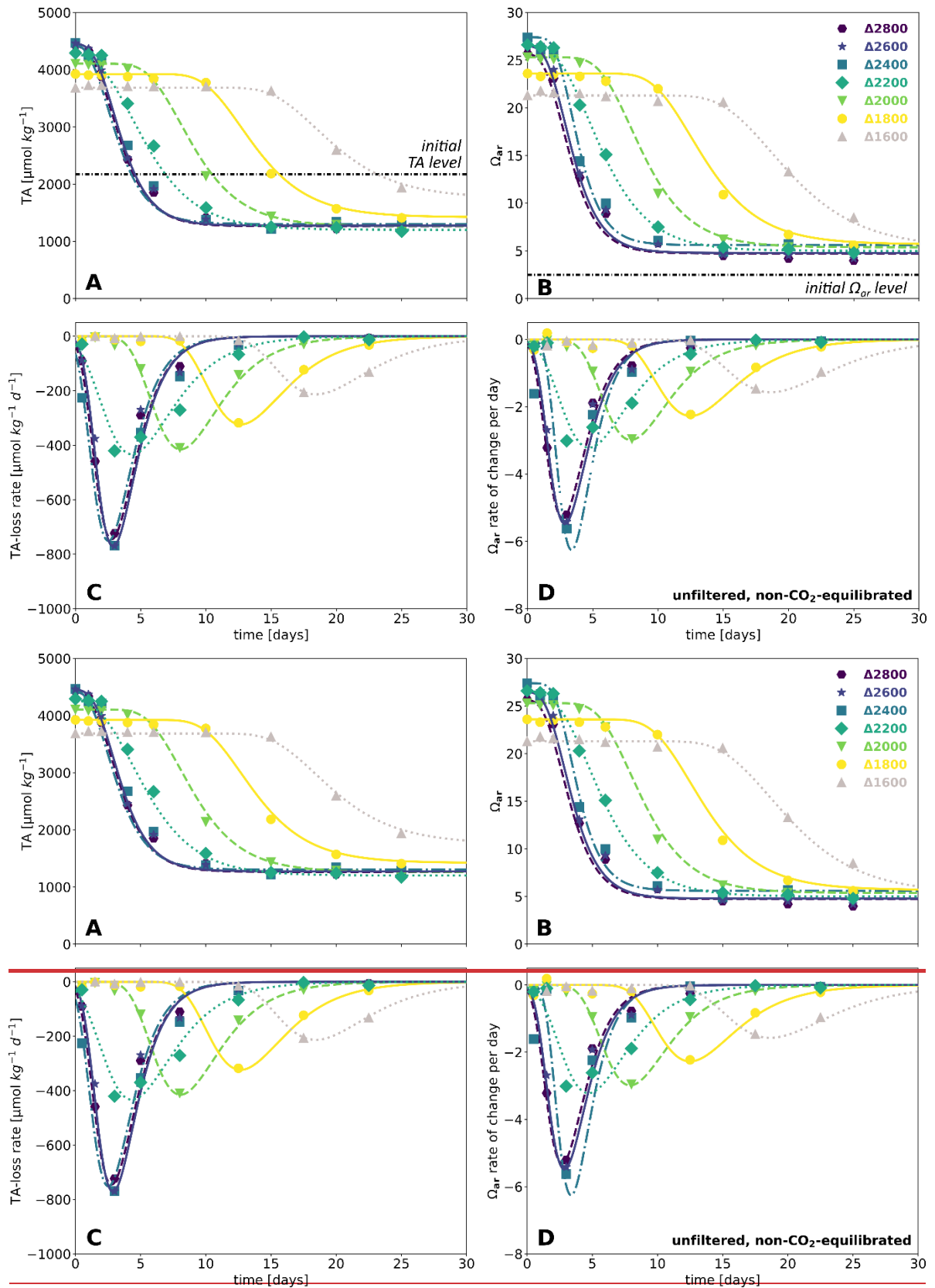


Figure 3: Results of the numerical curve fits – for the unfiltered neq approach, TA evolution over time (A),  $\Omega_{ar}$  evolution over time (B), TA-loss rate over time (C),  $\Omega_{ar}$  rate of change over time (D). *Line* plots: curve-fitted continuous functions, markers: measured data points, for related diagrams for filtered approaches see Figs. [S1](#), [S2](#) and [S3](#).

178 For the unfiltered neq experiment (Fig. 3), treatment levels  $\Delta TA_{1600}$  and higher entered into an APP after  
179 exceeding critical TA levels to initiate the runaway carbonate precipitation process. Treatments levels  $\Delta TA_{2400-}$   
180  $_{2600}$  exhibited a buffering as a consequence of magnesium hydroxide precipitation (see Badjatya et al., 2022;  
181 Ringham et al., 2024; Suitner et al., 2024; Varliero et al., 2024), which prevented an increase above  $\sim 4470 \mu\text{mol}$   
182  $\text{kg}^{-1}$  in TA and  $\sim 27.4$  in  $\Omega_{\text{ar}}$ . The buffering effects were not recognized within the fitting procedure and the first  
183 data point (after  $\sim 3$  min runtime) of each treatment level was set as the baseline.

184

### 185 3.2 Induction time and timespan of the APP

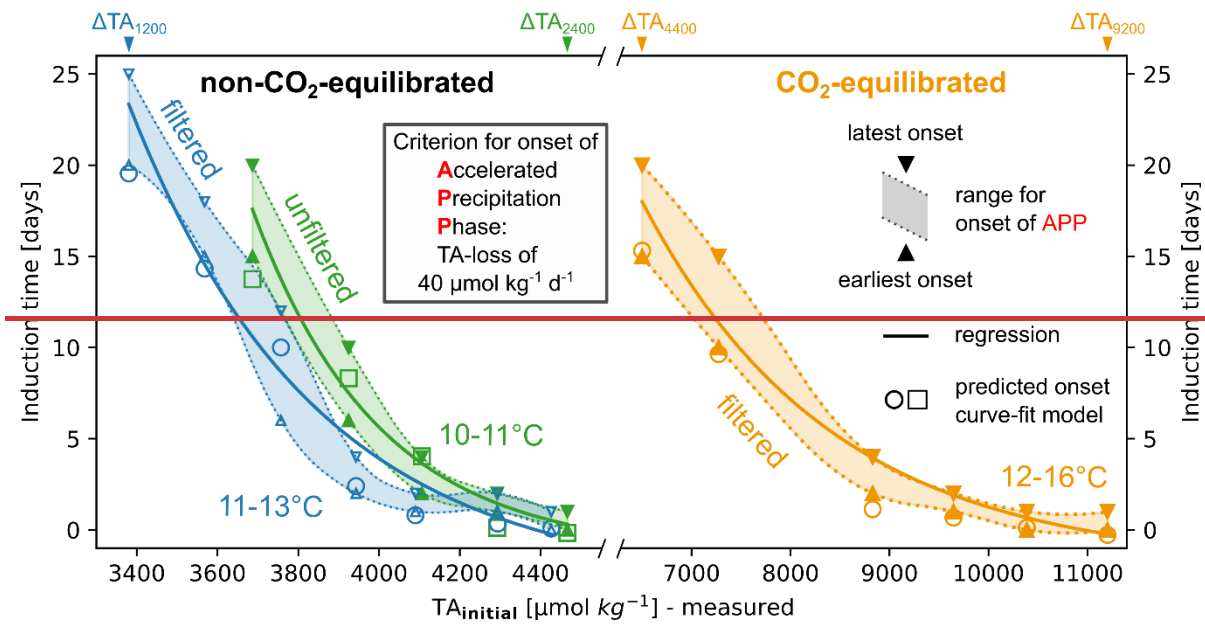
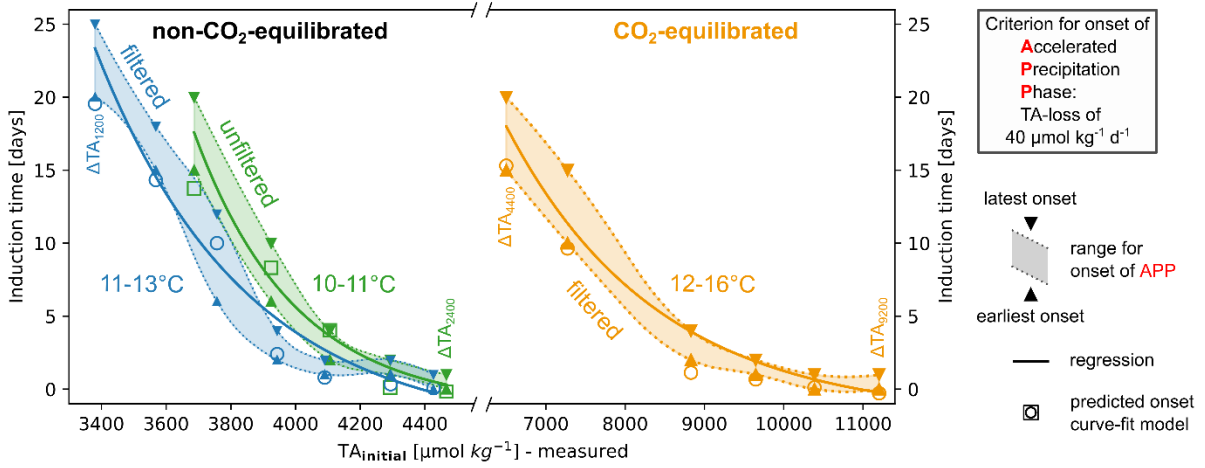
186 By employing the logistic curve fits, the temporal evolution of each approach could be parameterized. To identify  
187 the temporal stability ranges and reflect the transition from stable to precipitation-dominated system modes, a  
188 criterion of  $40 \mu\text{mol kg}^{-1} \text{d}^{-1}$  rate of change in TA was set. This rate provides a sufficiently high threshold to exclude  
189 a false detection due to natural variability or measurement errors, while still being low enough not to overlook  
190 a significant fraction of TA-alkalinity loss (see Fig. S11S9 for varying criteria).

191 Based on this criterion, Fig. 4 illustrates the induction times for the APPs. The shaded ranges indicate  
192 extrapolated timeframes between subsequent measurements during which the initiation of the APP for each  
193 treatment was detected. The displayed regressions were calculated using the averaged times from two  
194 consecutive measurement days. For comparison, hollow markers represent predictions from the presented  
195 curve-fitted functions. The regressions of the induction times uniformly follow an inverse exponential trend of  
196 the type:

$$197 \quad t(TA) = f e^{-g TA} - h \quad (5)$$

198 The employed data series covered a range of 25 days with progressively increasing induction times from 0 to 20  
199 days for treatments reaching  $\sim 4470$  ( $\Delta TA_{2400}$ ) to  $\sim 3380 \mu\text{mol kg}^{-1}$  ( $\Delta TA_{1200}$ ) in the filtered neq experiment and  
200  $\sim 11200$  ( $\Delta TA_{9200}$ ) to  $\sim 6500 \mu\text{mol kg}^{-1}$  ( $\Delta TA_{4400}$ ) in the filtered eq experiment. Treatment levels above  $\Delta TA_{2400}$  in  
201 the neq approaches exhibited an immediate onset of TA-loss due to the precipitation of secondary hydroxides  
202 and/or carbonate minerals, therefore, following the presented criterion, practically leading to their immediate  
203 entry into the APP process.

204 The same relationships and trends can also be applied using  $\Omega_{\text{ar}}$  as a variable. While the neq approaches exhibited  
205 lower  $\Omega_{\text{ar}}$  values (17.8-27.4) compared to the eq treatments (19.5-43.6), the onset of the APP in the neq  
206 experiments occurred significantly earlier. This indicates that  $\Omega_{\text{ar}}$  is not the only decisive factor guiding the  
207 (pseudo-) homogeneous nucleation process, determining the induction time.



208 Figure 4: Induction time for the onset of APP in relation to the initial TA addition level, based on the first detection of a TA-loss  
 209 rate of  $40 \mu\text{mol kg}^{-1} \text{d}^{-1}$ . Each pair of triangle markers represents two consecutive measurement days during which the set loss  
 210 rate criterion was met; hollow markers: predicted induction times for each treatment level, based on the introduced curve-fit  
 211 model. Exponential regression of average experimentally detected induction time, see Eq. (5) in Tab. 2 for related functions.

212

213 Table 2: Regressions of induction times, see Fig. 4. Note that the use of the given equation should not be generalized, as it is  
 214 only valid under the presented environmental conditions. Also be aware that the resulting predictions of induction times far  
 215 out of the specified TA addition ranges might not be accurate.

| $t(TA_{initial}) = f e^{-g TA_{initial}} - h$ (5) |            |            | Regression |               |       |                |
|---|------------|------------|------------|---------------|-------|----------------|
| Treatment   |            | Temp. [°C] | $f * 10^3$ | $g * 10^{-4}$ | h     | R <sup>2</sup> |
| non-<br>equilibrated                              | unfiltered | 10-11      | 2721.769   | 32.233        | 1.215 | 0.996          |
|   | filtered   | 11-13      | 39.633     | 21.646        | 2.972 | 0.977          |
| equilibrated                                      | filtered   | 12-16      | 0.603      | 5.243         | 1.934 | 0.988          |

216

### 217 3.3 Timespan of APP

218 To describe the temporal evolution of TA and  $\Omega_{ar}$  during the observed runaway processes for the present setups,  
 219 coefficients **(a)** and **(d)** in Eq. (1) can be set, while **(b)** could be evaluated by empirical or modeled data.  
 220 Consequently, only the duration of the APP represented by **(c)** needs to be estimated to enable the entire model  
 221 description of the precipitation procedure. The discrete nature of sampling days with decreasing frequency of  
 222 samplings towards the end of an experiment (up to 5 days) did not allow reliable empirical determinations of **(c)**.  
 223 The displayed APP timespans in Fig. 5 were therefore determined by the predictions of the presented curve-fits  
 224 (Fig. 3), based on the  $40 \mu\text{mol kg}^{-1} \text{d}^{-1}$  TA-loss criterion to define the start and endpoint of the APPs. Fig. 5  
 225 illustrates the related predicted timespans against the initially reached TA levels, categorized by the individual  
 226 experimental setups. The neq APPs form distinct clusters for each approach, which again can be subdivided into  
 227 treatments with and without the occurrence of immediate precipitation. Regardless of the initial TA  
 228 enhancement level, treatments that exhibited an immediate decline due to  $\text{Mg}(\text{OH})_2$  formation showcased  
 229 almost identical APP spans (unfiltered  $\sim 8.8$  and filtered  $\sim 5.9$ - $7.4$  days) within each approach. Although the neq  
 230 treatments without  $\text{Mg}(\text{OH})_2$  had the same starting conditions, the unfiltered experiments exhibited  
 231 approximately 4 days longer APPs. In APPs in the eq approach, the APPs showed a continuous decrease as the  
 232 initial TA addition levels increased, increase ranging from 5 to 11 days.

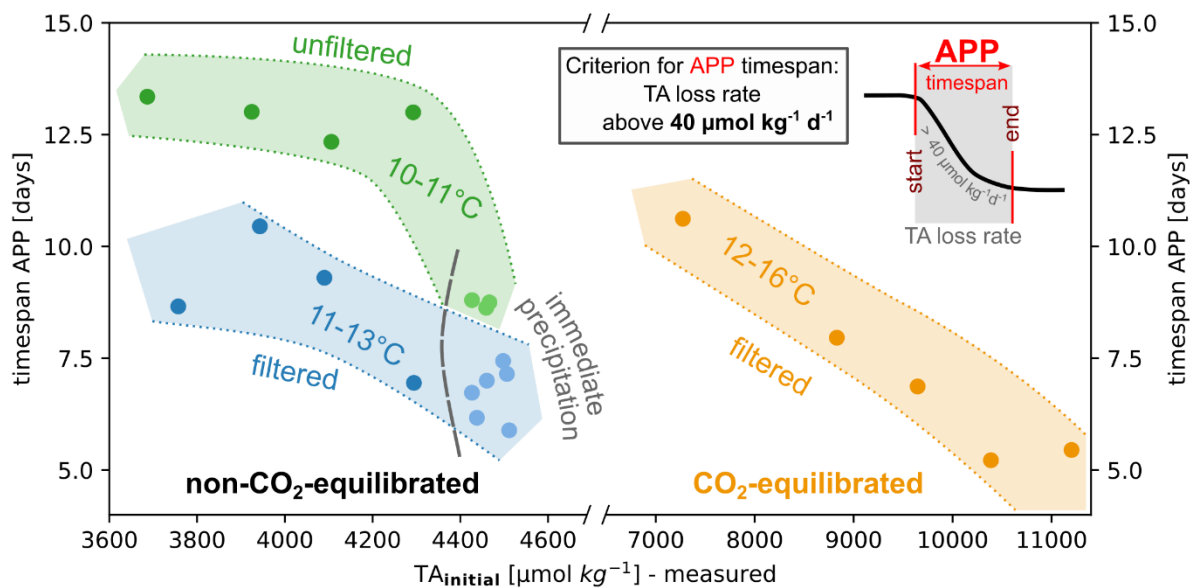


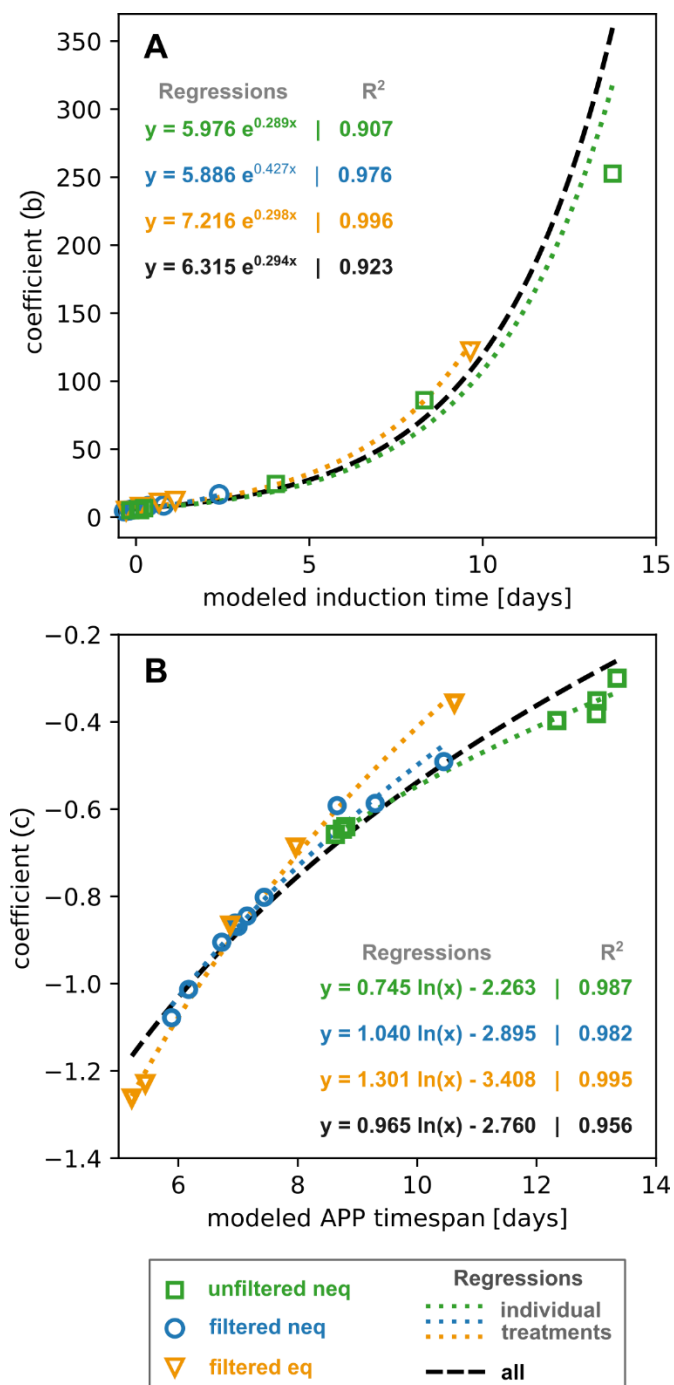
Figure 5: Overview timespans of APP in relation to the initial TA addition level; determined by the outcomes of the presented numerical logistic curve-fitting. Presented timespans are based on the introduced TA-alkalinity loss criterion (see section 3.2), which was defined as period with rates above  $40 \mu\text{mol kg}^{-1} \text{TA-loss d}^{-1}$ ; only treatments which reached the final stable stage were considered, neq treatments labeled with immediate precipitation showcased a loss of TA within the first 3 min of the experiment – most likely as a consequence of  $\text{Mg}(\text{OH})_2$  formation. (see Suiter et al., 2024)

### 233 3.4 Prediction of onset and timespan of APP

234 The established continuous logistic functions allow estimations of effects occurring between measurement  
 235 points, thereby improving the overall accuracy beyond what discrete experimental datasets could provide. Based  
 236 on the  $40 \mu\text{mol kg}^{-1} \text{d}^{-1}$  TA-loss criterion (see section 3.2 and sketch Fig. 5), these functions could therefore assess

237 the initiation of the APP for specific initial TA and/or  $\Omega_{ar}$  levels, as well as a given starting particle surface area (see  
 238 regressions in Fig. 4). In this regard, Fig. 6 illustrates the correlations of the curve-fitted coefficients **(b)** and **(c)**  
 239 and their related entities of the modeled induction times and APP timespans (see Fig. 2). Under the present  
 240 physicochemical conditions, the provided regressions could be utilized as conversion equations to estimate the  
 241 TA development of a treated water mass based on an existing database or to convert observational data into  
 242 mathematically expressible equations for predicting the future evolution. Note that the high correlations of  
 243 coefficients (b) and (c) with induction times and APP timespans are relate to the circumstance that both  
 244 coefficients are determined through the described numerical curve-fitting procedure, which is based on the  
 245 properties of the logistic function and thus indirectly incorporates information about induction times and APP  
 246 timespans.

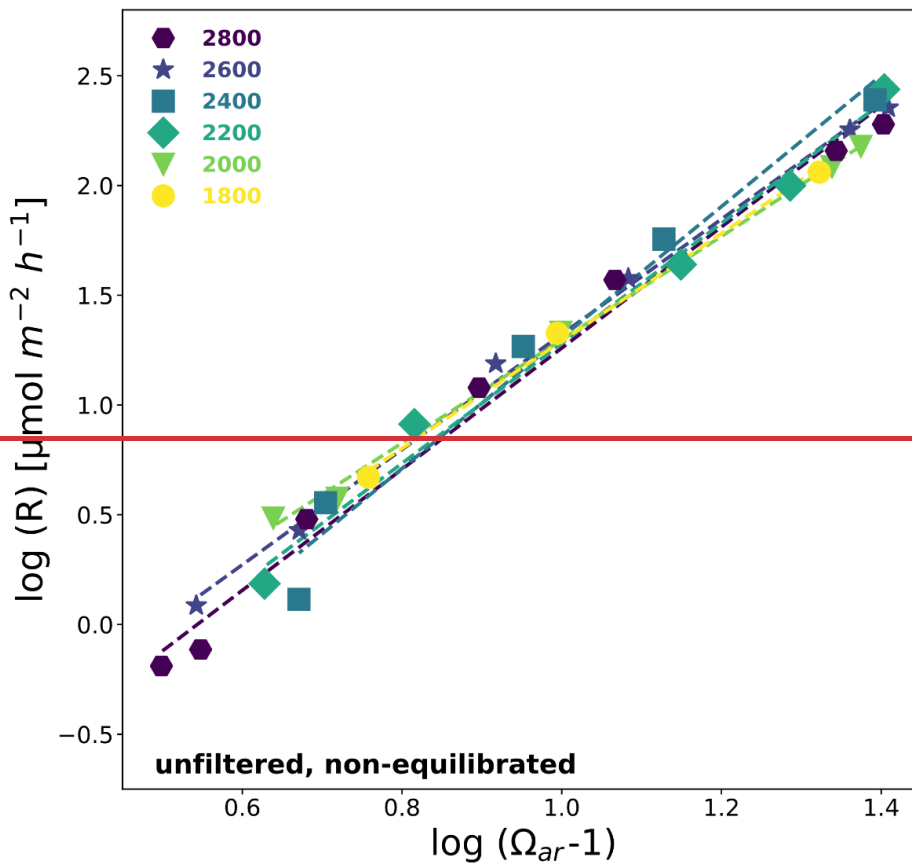
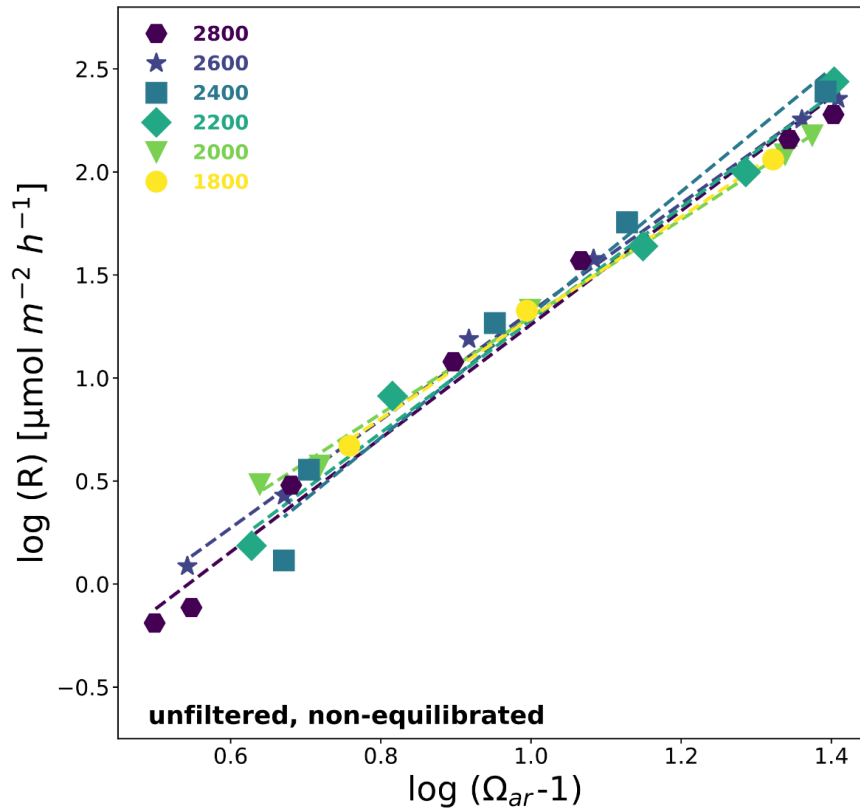
Figure 6: Regressions describing the relationships between the coefficient **(b)** and the modeled induction time [A], as well as the coefficient **(c)** and the modeled APP timespan [B] for each approach. The shown regressions allow for the conversion of specifiable time-dependent characteristics of a runaway process to the coefficients of the presented inverse logistic function (Eq. (1)). Specified relationships should not be generalized and are only valid within the given conditions of each approach.



247

### 248 3.5 Empirical rate equations

249 ~~Additional insights into~~ Further implications about the reaction speed and the ~~associated~~ related timespan of the  
250 APP can be ~~obtained through analysis of~~ provided by empirical rate law equations. As an example, Fig. 7  
251 ~~illustrates~~ demonstrates the relationship between the logarithm of TA-loss rates normalized ~~to the~~ by surface area  
252 and ~~the~~ aragonite saturation states for the unfiltered neq approach (see ~~Figs~~ Fig. S4 and S5 for details on ~~the~~  
253 filtered approaches), ~~focusing on~~ for treatments that entered the ~~APP accelerated precipitation phase~~. Throughout  
254 all experiments ~~the logarithm of the surface area normalized~~  $\log(R)$  TA-loss rates ~~R~~ ~~correlates~~ correlate with the  
255  $\log(\Omega_{ar}-1)$ , ~~in accordance with similar observations reported in literature (e.g. expressing the characteristic~~  
256 ~~relationship for carbonate formation (see Morse et al., 2007; Mucci & Morse, 1983; Zhong & Mucci, 1989). The~~  
257 ~~parameters n and k in Eq~~ The strong correlation of the linear regressions within each experiment enables the  
258 ~~articulation of the empirical rate equations, such as Eq. (2):  $R = k(\Omega_{ar}-1)^n$  were determined for each treatment~~  
259 ~~level in  $R = k(\Omega_{ar}-1)^n$ . In this work, as outlined in Eq (2) to (4) (section 2.3). Here,~~ equation R represents the  
260 surface area normalized TA-loss rate, ~~and k denotes~~ the rate constant.  
261 ~~The and n the reaction order. The related~~ values for n and  $\log(k)$  derived from the linear regressions ~~in the~~  
262 ~~unfiltered neq treatments~~ are provided in Tab. 3 (see ~~Tab. S4~~ Tab. S1 and ~~S5~~ S2 for filtered experiments). ~~These~~  
263 ~~values demonstrate), showing~~ reasonable consistency in n and  $\log(k)$  ~~values~~ within each of the three separate  
264 experiments. ~~Treatment levels influenced by the~~ While some treatments, ~~showing~~ immediate ~~formation of~~  
265 ~~Mg(OH)<sub>2</sub> as pH approached approximately 10.3 show minor deviations)~~ formation, ~~slightly deviate~~, the  
266 ~~remaining~~ other treatment levels ~~exhibit~~ displayed reaction orders (n) within a relatively narrow range of 2.45 to  
267 2.73. In comparison,  $\log(k)$  values ranged between 0.30-1.68, showcasing a higher variability.



268 *Figure 7: Carbonate precipitation kinetics for unfiltered neq treatments that entered the APP; see Tab. 3 for related regressions*

269 *and rate equations.*

270

271 Table 3: Overview of coefficients and regressions of empirical rate equations for unfiltered neq treatments, also see Fig. 7 and  
 272 [Tab. S6 for cross-comparison of all treatments.](#)

| Treatment   | $\log(R) = n(\Omega_{ar} - 1) + \log(k)$ |        |                |                |
|-------------|--|--------|----------------|----------------|
|             | n  | log(k) | R <sup>2</sup> | $\hat{\sigma}$ |
| <b>2800</b> | 2.76                                     | -1.50  | 0.989          | 0.117          |
| <b>2600</b> | 2.62                                     | -1.30  | 0.997          | 0.055          |
| <b>2400</b> | 2.98                                     | -1.68  | 0.975          | 0.167          |
| <b>2200</b> | 2.73                                     | -1.45  | 0.989          | 0.106          |
| <b>2000</b> | 2.35                                     | -1.06  | 0.997          | 0.046          |
| <b>1800</b> | 2.45                                     | -1.16  | 0.996          | 0.060          |
| <b>all</b>  | 2.68                                     | -1.39  | 0.985          | 0.106          |

273

### 274 3.6 Evolution of particles and sinking speed

275 To assess the impact of secondary precipitated particles during OAE approaches, precipitated materials from the  
276 studies by Hartmann et al. (2023) and Suitner et al. (2024) were analyzed for shape, size, and sinking velocity. As  
277 qualitatively depicted in ~~these studies, the study of Suitner et al. (2024) (see Fig. 7 therein)~~ the aragonite  
278 precipitates manifest and evolve in a variety of forms and sizes, ranging from stem-like structures, followed by  
279 double-broccoli shapes and ultimately forming closed spheres (see Fig. 8).

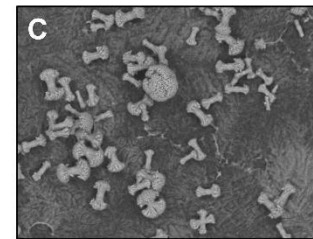
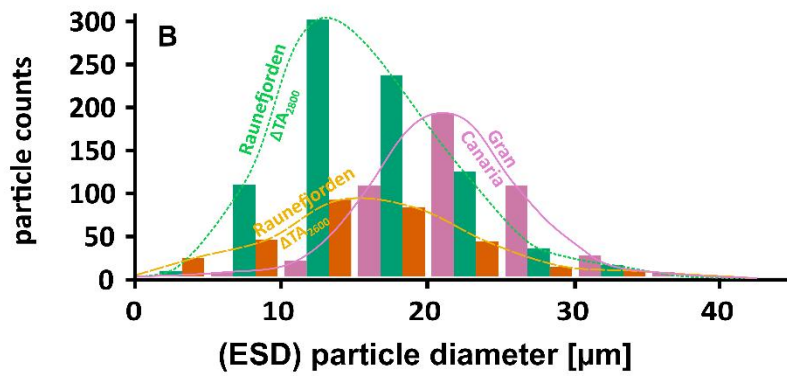
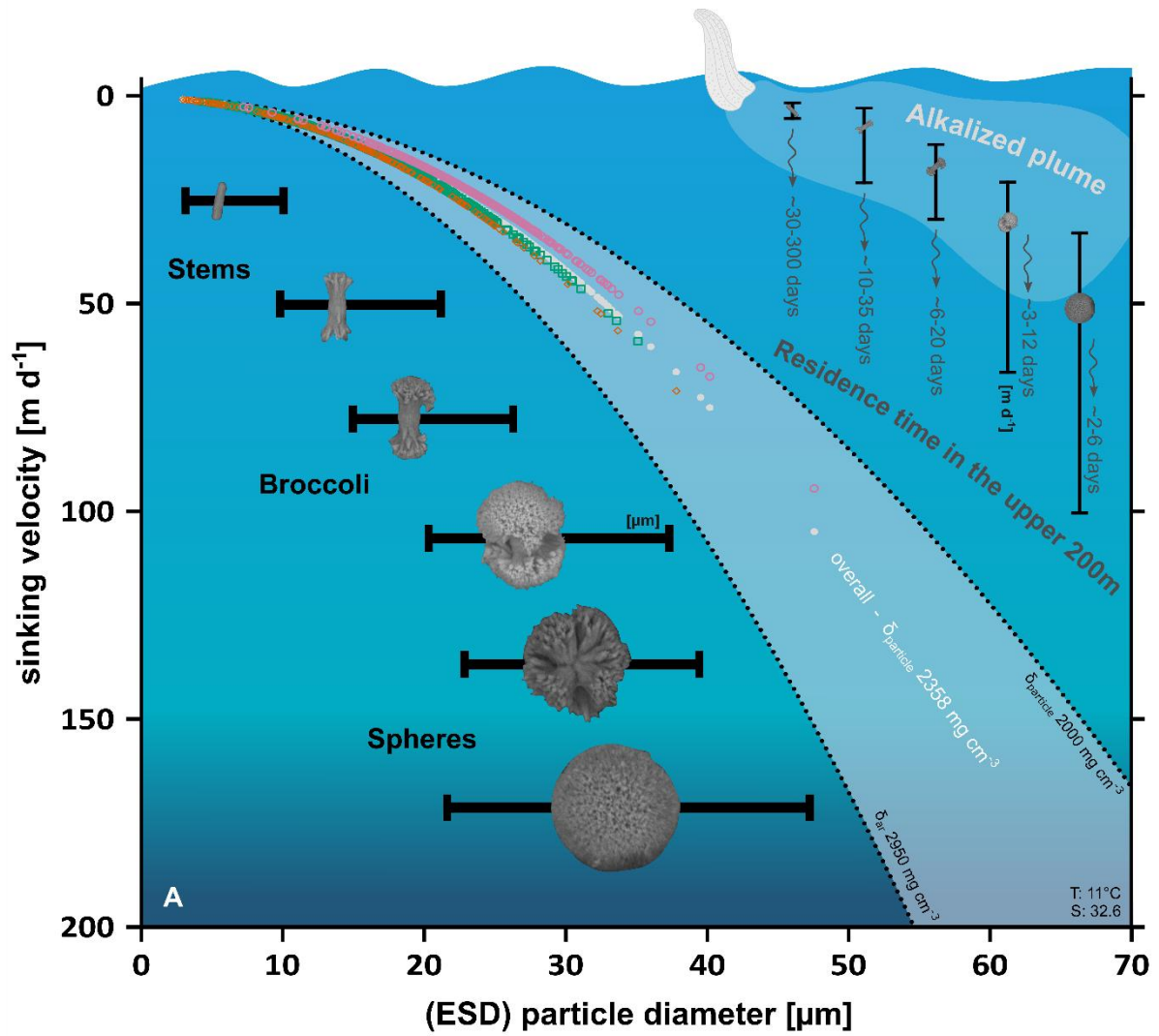
280 For this study the length and width distribution of 950 precipitated particles were determined by manual  
281 inspection of four overview SEM images (see Fig. ~~S7S4~~) from Gran Canaria samples (see Hartmann et al., 2023  
282 for details; analyzed treatment level:  $\Delta TA_{2400}$ , filtered, neq, Temp.  $\sim 23^\circ\text{C}$ , Sal.  $\sim 36.5$ , runtime 4 days) and the  
283 Raunefjorden, Bergen (this study and Suitner et al., 2024, see Figs. 3 and 7 therein; analyzed treatment levels:  
284  $\Delta TA_{2800}$  and  $\Delta TA_{2600}$ , Temp.  $\sim 11^\circ\text{C}$ , Sal. 32.6, runtime 25 days – highest unfiltered neq treatments). Results of this  
285 evaluation are provided in Fig. ~~S8S6~~. Length and width distributions of the formed particles follow distinct ratios,  
286 allowing the definition of three categories: **1.** Stems ( $<0.5$ ), **2.** Broccoli ( $0.5 < x < 0.9$ ) and **3.** Spheres ( $>0.9$ ). Note  
287 that this method also categorizes regularly shaped, multi-branched particles as spheres (see Fig. 8). Precipitates  
288 from the Gran Canarian campaign primarily comprised well-developed broccoli and spherical-shaped particles,  
289 whereas the samples from the Raunefjorden were characterized by less evolved stems and broccoli as the  
290 dominant components. Although the runtime for the Gran Canarian sample was considerably shorter (4 days) in  
291 comparison to the Raunefjorden (25 days), the  $\sim 12^\circ\text{C}$  difference in temperature led to significantly higher  
292 precipitation rates and more developed shapes. The analyzed Raunefjorden samples originate from the same  
293 experiment and differ only in the initially added TA-level of  $200 \mu\text{mol kg}^{-1}$ . Even this minor difference in TA  
294 addition resulted in the presence of more evolved shapes in the higher treatment.

295 ~~The gravitational sinking velocities of precipitated particles were measured using a FlowCam setup (see Bach et~~  
296 ~~al., 2012 for technical details).~~ Based on the ~~concept~~ distributions of equivalent spherical diameters (ESD) the  
297 ~~density of each particle was~~ sinking velocities of the precipitated materials were calculated, ~~revealing a range~~  
298 ~~from to identify their hypothetical sinking velocities. To facilitate this calculation, the densities of the aragonite~~  
299 ~~precipitates were determined by actual sinking velocity measurements of the same materials, providing densities~~  
300 ~~of  $1.54$  to  $3.18 \text{ g cm}^{-3}$  for  $^{-3}$  in an ESD sizes between range of  $12$  and  $50 \mu\text{m}$ . The average density was determined~~  
301 ~~to be  $2.358 \text{ g cm}^{-3}$ .~~ The discrepancy with the density of aragonite ( $\sim 2.95 \text{ g cm}^{-3}$ ) may result from an overestimation  
302 of particle sizes in the calculation method, which relies on an inversion of Stokes' Law for the terminal sinking  
303 velocity of perfect spheres. However, most particles are ~~non-not~~ spherical and contain numerous internal cavities  
304 within their structure (see Fig. S7), and their densities are therefore expected, ~~which likely contributes to be~~  
305 ~~lower than those an underestimation of pure aragonite. The determined particle density was then used to~~  
306 ~~calculate the theoretical sinking velocities of the manually counted precipitated particles. To account for~~  
307 ~~potential variability in particle density, Fig. densities. Therefore, Fig. 8 presents features~~ a range of sinking  
308 velocities of the counted precipitates.

309 ~~in dependence to a variable density, supported by ESD distributions and ranges for different types of precipitated~~  
310 ~~particles.~~ Measured sinking velocities for precipitated particles within the aforementioned density range varied  
311 from  $\sim 5 \text{ m d}^{-1}$  ( $14 \mu\text{m}$  particle) to  $\sim 47 \text{ m d}^{-1}$  ( $41 \mu\text{m}$  particle). Recorded particles in the ESD range of  $50$ -  
312  $180 \mu\text{m}$  were not included in the calculations, as they were not observed within the same filter material that

313 was analyzed by visual inspection, ~~yielding densities of 1.1–1.3 g cm<sup>-3</sup>~~. Discrepancies between measured and  
314 calculated values may reflect aggregation effects ~~or for very high values and the~~ technical limitations of the  
315 utilized FlowCam to track particles smaller than 3 ~~µm~~ (Bach et al., 2012).  
316 Derived from the calculated sinking velocities, the residence times within the upper 200 m of the water column  
317 were determined. Accordingly, under idealized conditions, early precipitated stages, such as stems (<10µm),  
318 could remain for a few months within the upper ocean layer, providing potential additional surfaces for an  
319 ongoing ~~heterogeneous~~ heterogeneous precipitation if a continuous local alkalization is applied. In contrast,  
320 precipitates >30 µm would descend within days to deeper ocean layers, not affecting the precipitation behavior  
321 of continuous surface alkalization attempts. Notice that sinking velocities are temperature and salinity  
322 dependent, and therefore would vary under different environmental conditions (see Fig. [S9](#)).





Example SEM filter of carbonate precipitates and their variety of shapes (for further details see Fig. S1)

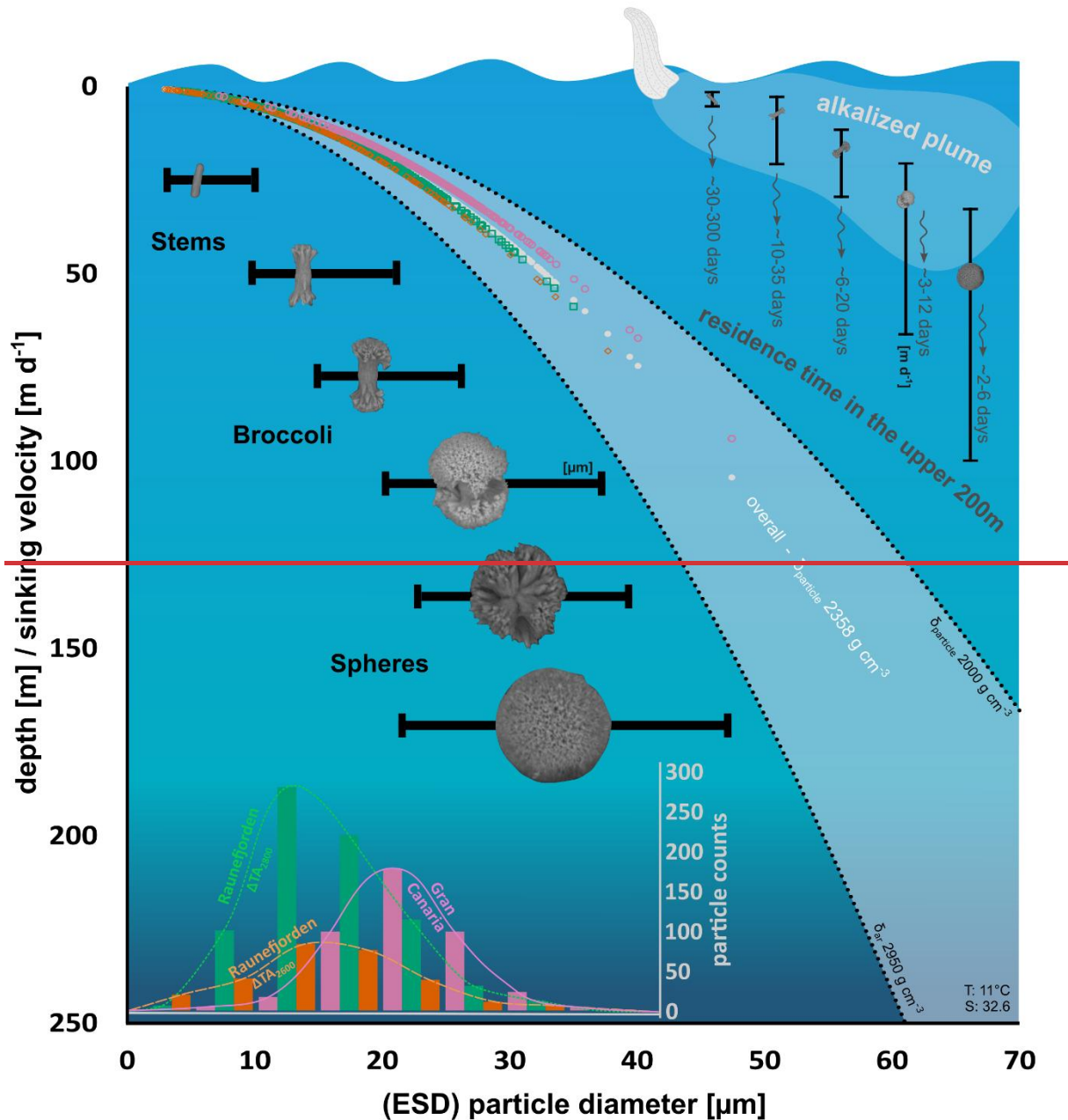


Figure 8: (A) Calculated sinking velocities of particles (hollow markers) as a function of ESD for each treatment (green squares: neq unfiltered  $\Delta\text{TA}_{2800}$  – Raunefjorden, Bergen; orange diamonds: neq unfiltered  $\Delta\text{TA}_{2600}$  Raunefjorden, Bergen; pink circles: neq filtered  $\Delta\text{TA}_{2400}$  Gran Canaria). ESD distribution The mean time range for average particles of stem their class (stems, broccoli and sphere shaped precipitates (horizontal) and their calculated mean residence time in spheres) to sink below the mixed layer depth (assumed to be 200 m), neglecting particle growth processes (B) related particles counts in size fractions of  $5 \mu\text{m}$ , also see Fig. S8 for length:width distribution (C) example section of a SEM filter ( $\Delta\text{TA}_{2600}$  Raunefjorden), see Fig. S7 for complete set of all filters.

## 325 4 Discussion

### 326 4.1 General findings

327 By analyzing the experimental datasets provided by Suitner et al. (2024), this study demonstrates that the  
328 process of ~~TA-alkalinity~~ loss during runaway carbonate precipitation follows quantifiable relationships. For the  
329 present study, the compiled concepts allowed the description of the principles guiding the entire runaway  
330 process. The obtained capability to predict TA-stability ranges, in terms of time and magnitude, might help  
331 ~~prevent~~~~preventing~~ secondary mineral formation, thereby optimizing the assessments for OAE application  
332 scenarios. Furthermore, the simplicity of the logistic curve fit model, along with the demonstration that the  
333 carbonate precipitation follows simple rate law equations (see Morse et al., 2007; Mucci & Morse, 1983; Zhong  
334 & Mucci, 1989), might facilitate the straightforward integration of these fundamental mechanisms into ocean  
335 models like the studies by He & Tyka (2023), Ou et al. (2025), Schwinger et al. (2024), Wang et al. (2022) or Zhou  
336 et al. (2024).

337

### 338 4.2 Nucleation and onset of accelerated precipitation phase

339 Previous studies examining the evolution of the runaway precipitation process in the context of OAE (Hartmann  
340 et al., 2023; Moras et al., 2022, 2024; Suitner et al., 2024) observed and described considerable periods with  
341 stable TA levels before the onset of the APP (~~e.g.~~-see Fig. 1 ~~modified after Suitner et al., 2024~~), depending on the  
342 ~~TA~~alkalinity and DIC levels.

343 In theory, even at natural background supersaturation levels in the ocean, (pseudo-)homogeneous precipitation  
344 is expected to occur at very slow rates, on timescales of thousands of years (Pytkowicz, 1965, 1973). Regardless,  
345 the nucleation and precipitation processes in ocean waters are suppressed by inhibitory species like  $Mg^{2+}$   
346 (Berner, 1975; Pan et al., 2021; Pokrovsky, 1998), phosphate- (Burton & Walter, 1990) or dissolved organic  
347 matter (Chave & Suess, 1970; Kellock et al., 2022; Moras et al., 2024). Naturally occurring precipitation events in  
348 the ocean are associated with unique occurrences such as flash floods (Wurgaft et al., 2016, 2021) or ~~observed~~  
349 ~~during whiting events~~whittings (Broecker & Takahashi, 1966; Bustos-Serrano et al., 2009; Morse et al., 2003),  
350 providing high degrees of (re)suspended sediments that catalyze a heterogeneous carbonate precipitation  
351 procedure.

352 To consider the persistent (pseudo-)homogeneous precipitation within typical natural seawater supersaturation  
353 ranges, the terminology concerning specific stability ranges of TA or timeframes for the onset of secondary  
354 carbonate formation should be refined. However, within typical observation times in the Earth system, the  
355 precipitation of secondary calcium carbonate in particle-free seawater solutions is expected to be suppressed to  
356  $\Omega_{ar}$  values of approximately 11.3 or below (derived from Eq. (4) in Marion et al. (2009), based on data by Morse  
357 & He (1993) and Morse et al. (2007)).

358 Nevertheless, even a  $0.2\mu m$ -filtered natural seawater contains around  $\sim 10^9$  particles per ml in the size range of  
359 5-120 nm, already offering a total surface area of around  $8 m^2$  per  $m^3$  (cf. Wells & Goldberg, 1992), potentially  
360 acting as a catalyst to initiate carbonate precipitation in alkalinity treated seawater. In the presence of surfaces

361 for pseudo-homogeneous/ heterogeneous [precipitation](#) such as suspended sediments, colloids, organic matter  
362 or the introduced solid alkalization substrates, Moras et al. (2022) reported an  $\Omega_{ar}$  threshold of ~5-7 for the  
363 observable onset of carbonate formation for the given runtime of the experiment. Potentially, the colloidal  
364 structure of  $Mg(OH)_2$  precipitates (see Badjatya et al., 2022), typically formed above pH values of ~10.5 as a  
365 consequence of [TAalkalinity](#) addition (cf. Eisaman et al., 2023; Haas, 1916; Kapp, 1928; Suitner et al., 2024;  
366 Varliero et al., 2024) could serve the same purpose and lower the threshold for carbonate precipitation.  
367 However, the redissolution of the formed  $Mg(OH)_2$  through the mixing and dilution processes, as described by  
368 Ringham et al. (2024), may inhibit this effect and would also allow much higher short-term pH and TA  
369 concentrations around an alkalinity injection site when using liquid stock solutions.

370 To characterize the transition from a state with negligible shifts in carbonate chemistry towards a phase primarily  
371 driven by carbonate formation, (cf. [Suitner et al., 2024](#)), a practicable criterion of a  $40 \mu\text{mol kg}^{-1} \text{d}^{-1}$  TA-loss was  
372 set to determine the start of the intensified precipitation stage (see Figs. 4 and 5). This criterion was also used to  
373 describe the induction time, which is the period before a measurable onset of secondary carbonate formation  
374 can be detected (Fig. 4). Since the induction time includes a fundamental uncertainty, it does not reflect an  
375 intrinsic property of the treated solution itself and relies on the detection capability of the experimental setup  
376 (Söhnel & Mullin, 1988) and might be chosen differently in future work (see Fig. [S11S9](#) for varying criteria). While  
377 the selected criterion already depicts relatively high loss rates, it enables detectable changes, distinguishable  
378 from measurement uncertainties or natural variabilities. The overall emerging patterns related to the onset and  
379 duration of the APP nevertheless remained relatively consistent across different tested threshold values.

380

### 381 **4.3 Predictability of the runaway process**

382 The consistent patterns during the [TA-alkalinity](#)-loss within all three experimental setups allowed the  
383 introduction of continuous and differentiable functions for each treatment level, enabling further analysis to  
384 examine relevant factors guiding the runaway process. Fuhr et al. (2022) utilized a comparable inverted logistic  
385 function to model the process of secondary carbonate formation during olivine dissolution experiments in  
386 seawater. However, the model was not consistently applied to describe a runaway carbonate precipitation  
387 process nor used as a general predictive model to determine the stability ranges of the added [TAalkalinity](#) in OAE  
388 approaches.

389 The characteristics of the logistic function applied in this study, facilitate the conversion of both empirically  
390 determined and hypothetical parameters, such as induction time, duration of the APP (Fig. 5), or the initial and  
391 final TA levels before and after the runaway process. The applicability of kinetic rate equations, combined with  
392 the ability to quantify the precipitation process, enables a description and prediction of the temporal evolution  
393 of the carbonate formation. This may facilitate the integration of the [TAalkalinity](#) depletion procedure into  
394 various predictive modeling approaches. Although these statements currently apply only under the tested  
395 environmental conditions, they nonetheless suggest the general capability to assess a framework for guiding  
396 time and TA level ranges in OAE approaches. Since the logistic model is based on experimental data from bottle  
397 experiments, processes such as the removal of surface area due to the sinking of precipitated carbonate particles  
398 were not accounted for - see section 4.6 for an approach to address this topic.

399 Under specified temperature and salinity conditions, as well as predefined TA/DIC levels after OAE treatment  
400 and an estimated final  $\Omega_{ar}$  after the precipitation process stopped (typically  $\sim 1.5$ - $5.0$ , see Fuhr et al., 2022;  
401 Hartmann et al., 2023; Moras et al., 2022; Pan et al., 2021; Suitner et al., 2024), the resulting total TA-loss can be  
402 computed. This calculation follows the condition that the ~~TA-alkalinity~~ loss reflects the ideal 2:1 TA:DIC ratio  
403 during carbonate mineral precipitation in seawater (Zeebe & Wolf-Gladrow, 2001). Given these assumptions,  
404 upper and lower limits of the logistic function (coefficients **(a)** and **(d)**, Eq. (1)) can be determined. To characterize  
405 measures such as induction time (coefficient **(b)**) and the duration of the APP (coefficient **(c)**), it is necessary to  
406 acquire empirical data that account for the specific conditions of the deployment area. These data could either  
407 be provided by actual experiments or model predictions, based on a comprehensive database which accounts  
408 for broad ranges of TA, DIC, temperature, salinity, and practical available surface area, as well as inhibitory factors  
409 or potential effects of biota. To validate the predicted precipitation behavior, additional gradient experiments  
410 need to be conducted to better understand the geochemical reaction pathways.

411

#### 412 **4.4 Empirical rate equations using $\Omega_{ar}$ and particle surface area during APP**

413 After passing the induction time to start the detectable carbonate formation process by (pseudo-/)homogeneous  
414 precipitation and overcoming the delaying inhibition effects (Marion et al., 2009; Morse & He, 1993; Schulz et  
415 al., 2023), the triggered heterogeneous precipitation can be described by basic empirical rate equations (Fig. 7,  
416 S4 and S5). These equations demonstrate the fundamental role of  $\Omega_{ar}$  as a guiding factor for the precipitation  
417 process. The kinetics of carbonate formation remained relatively consistent across all treatment levels within  
418 each experimental approach (see Tabs. 3, ~~S4S1~~ and ~~S5S2~~). The observed consistent correlations between  
419 saturation states and surface area normalized precipitation rates indicate that the runaway carbonate formation  
420 processes during the present incubations followed the known kinetics of heterogeneous carbonate formation in  
421 seawater (cf. Morse et al., 2007; Zhong & Mucci, 1989).

422 Fig. 9 illustrates the role of  $\Omega_{ar}$  saturation states and generated ~~particle~~ surface area in guiding the ~~TA-alkalinity~~  
423 loss rates during the precipitation process. The black ~~linegraph~~ represents the curve fit of TA-loss rates of the  
424 unfiltered neq  $\Delta TA_{2000}$  approach; the experimentally determined rates are indicated by black triangles (~~also seeef.~~  
425 Fig. 3c). Assuming that the entire lost ~~TAalkalinity~~ was transformed into aragonite precipitates with a surface  
426 area of  $2.283 \text{ m}^2 \text{ g}^{-1}$  (see ~~sectionchapter~~ 2.3), the total generated particle surface area (PSA) could be determined  
427 (red, ~~dash-~~dotted ~~linegraph~~). The overall expected TA-loss rate per  $\text{m}^2$  (brown, dashed ~~linegraph~~) was obtained  
428 by utilizing the empirical logistic curve fit for the temporal evolution of  $\Omega_{ar}$  (Fig. 3b), normalizing it to  $1 \text{ m}^2$  surface  
429 area, and inserting it into the rate equation (Eq. (4)). Given that the system initially exhibits a negligible degree  
430 of PSA, the relatively high precipitation potential by the  $\Omega_{ar}$  saturation state does not result in a measurable TA-  
431 loss rate. Following the presented concept, the consistently high  $\Omega_{ar}$  values led to a continuous (pseudo-  
432 /)homogeneous precipitation during the induction time, thus causing a rise in PSA until the system shifts to  
433 heterogeneous precipitation, and ultimately resulting in a detectable exponential runaway process. The interplay  
434 of precipitation potential by  $\Omega_{ar}$  and the practical available surface area could therefore be determined as the  
435 primary factors guiding the actual observed TA-loss rates.

436 Within the uncertainties of the applied calculation steps and methods, the practical TA-loss rate could simply be  
437 described as the product of these two factors. To visualize this relationship, the dotted light blue line in Fig. 9  
438 represents an empirical rate law equation that combines the shown PSA (red, dash-dotted line) and the surface  
439 normalized expected precipitation rate (brown, dashed line) with the determined rate constant (k) and reaction  
440 order (n) for the  $\Delta TA_{2000}$  treatment (see Tab. 3). The shape of the resulting function traces the measured TA-loss  
441 rates (black triangles) within reasonable accuracy (see Fig. S10 for other treatments). Be aware that any kind of  
442 inhibition effect is incorporated in the underlying experimentally determined temporal TA evolution which  
443 represents the basis for all shown parameters (also see Fig. S8 for other treatments). For comparison, the blue  
444 data points in Fig. 9 represent the calculated theoretical loss rates at each sampling day, by inserting the  
445 experimentally determined  $\Omega_{air}$  and PSA values into the related empirical rate equation for  $\Delta TA_{2000}$  (see Tab. 3).  
446 As this equation does not account for any inhibitory factors, the resulting rates exhibit a slight positive bias  
447 compared to the observed values.

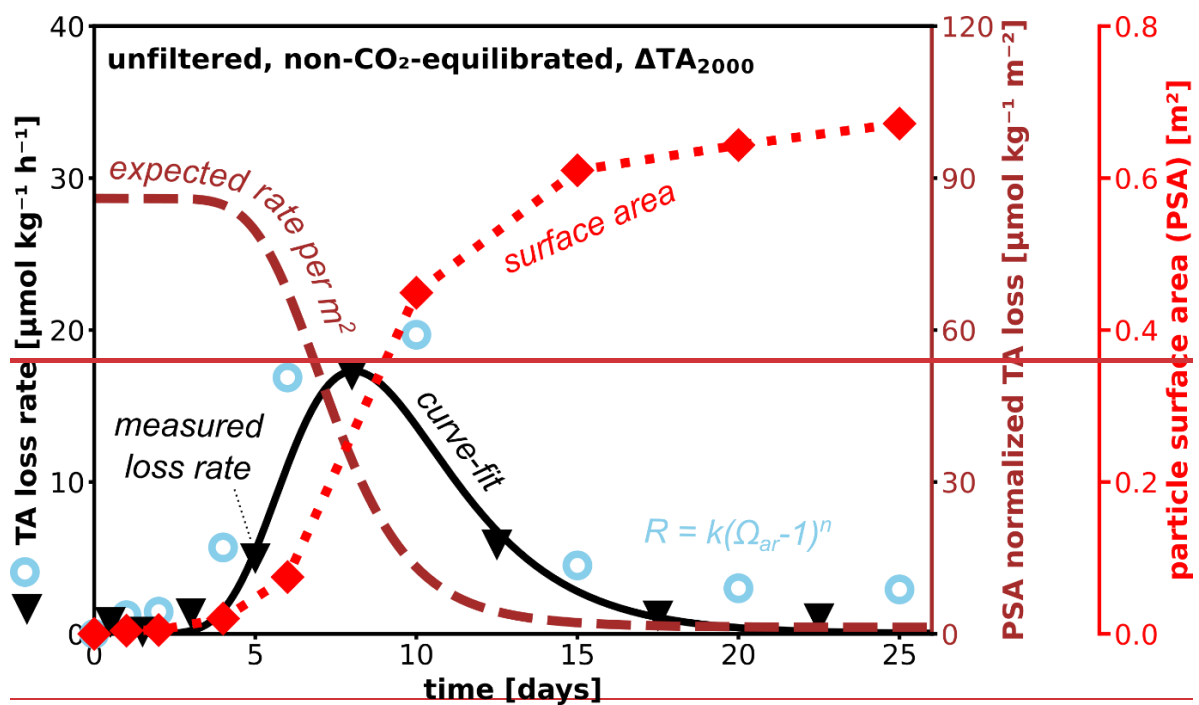
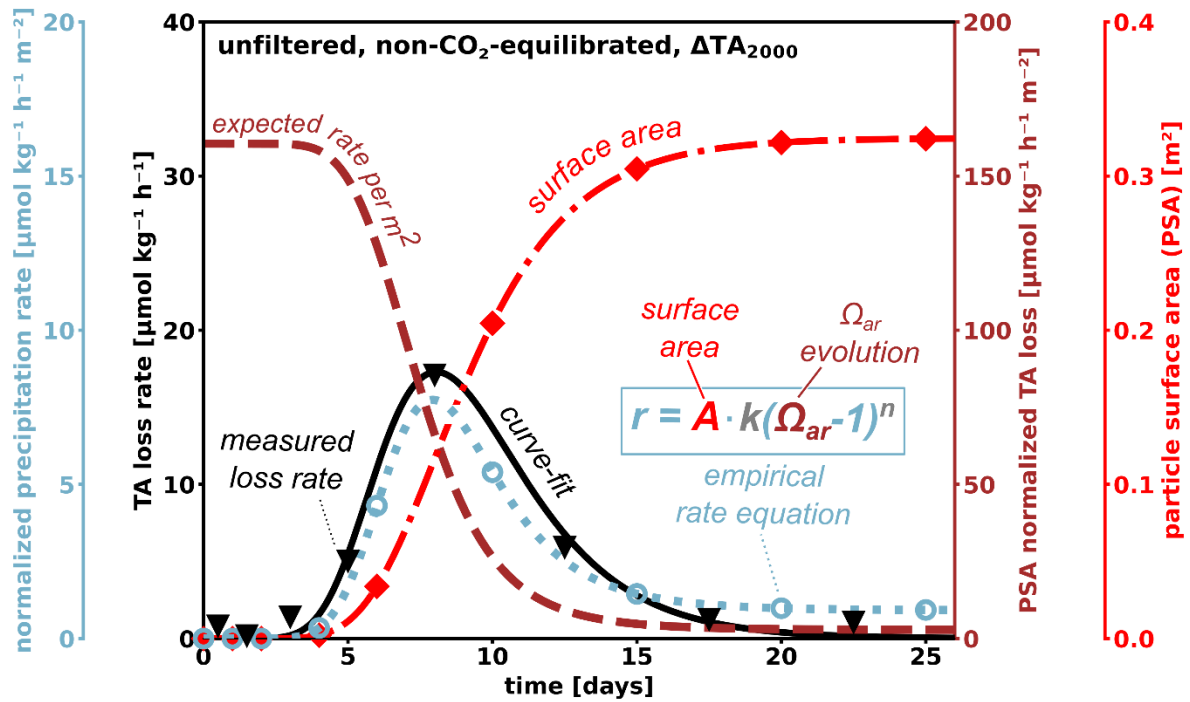


Figure 9: Conceptual figure, illustrating the interplay of  $\Omega_{ar}$  and particle surface area guiding the TA-loss rate evolution (dashed, **brown** & **dark-red**). After TA injection high  $\Omega_{ar}$  values provide a high potential for the formation of carbonates by heterogeneous precipitation. In the absence of existing particle surface area (red **dash-dotted**), (pseudo-)homogenous precipitation would dominate the period until the start of the APP and the resulting runaway precipitation process. Observed TA-loss rates (black triangles) are therefore a combination of the available practical surface area and the precipitation potential by  $\Omega_{ar}$  oversaturation. The related empirical rate equation (dotted, light blue) connects these two factors with the determined rate constant ( $k$ ) and reaction order ( $n$ ), tracing the shape and symmetry of the measured TA-loss rate. Hollow light-blue markers provide the output of the related empirical rate equations for each sampling day. While the potential to precipitate carbonates decreases with progressive precipitation, additional surface area is generated. The symmetry of the TA loss rate can be mathematically described with good approximation using only these two factors:

Understanding how long particles remain in a critical zone to maintain a full-grown runaway process is therefore relevant for future considerations. ~~Hollow light blue markers provide the output of the related empirical rate equations for each sampling day.~~ The shown TA and loss rate data are taken from the empirical data sets for the neq unfiltered  $\Delta TA_{2000}$  approach, see Fig. [S10S4](#) for other treatments levels.

448

#### 449 **4.5 Could a runaway process be triggered in an open world context?**

450 Mixing with untreated water around an injection point may lead to an efficient dilution below non-critical  
451 ~~TAalkalinity~~ levels within seconds to minutes. Such a process would effectively prevent ~~TAalkalinity~~ leakage, as  
452 described in this study, which assumes that the formed particles act as catalysts for future precipitation. This is  
453 supported by findings from a mesocosm experiment and corresponding side experiments, where the presence  
454 of additional suspended aragonite particles accelerated the ~~TA-alkalinity~~ loss (Paul et al., 2024). In contrast, fresh  
455 seawater enhanced to the same TA-levels did not show any ~~TA-alkalinity~~ loss within 10 days in their experiments.  
456 These observations indicate that free-floating particles in the water column can accelerate heterogeneous  
457 precipitation in a runaway style.

458 Precipitation events can be triggered naturally without additional treatment, especially for locations with already  
459 relatively high  $\Omega_{ar}$  background levels, for example, due to high evaporation rates (Bialik et al., 2022) or high  
460 degrees of (re)suspended sediments present on carbonate platforms (Broecker & Takahashi, 1966; Bustos-  
461 Serrano et al., 2009; Morse et al., 2003), or close to river mouths (Wurgaft et al., 2016, 2021) providing additional  
462 PSA to catalyze precipitation events. Under inappropriate ~~TAalkalinity~~ deployment circumstances, secondary  
463 mineral formation might be triggered locally around injection sites, within short timescales. Moras et al. (2022)  
464 suggested that visible APP starts around  $\Omega_{ar}$  of 5, which translates for the mostly particle-free water of the  
465 Raunefjorden into  $\Delta TA \sim 245 \mu\text{mol kg}^{-1}$  applying a neq OAE approach and  $\Delta TA \sim 580 \mu\text{mol kg}^{-1}$  for an eq OAE  
466 approach. The induction time before the APP begins can be estimated using Equation (5), based on the specified  
467 TA-loss criterion of  $40 \mu\text{mol kg}^{-1} \text{d}^{-1}$ . For these configurations, the projected induction times would be 1074 days  
468 and 143 days, respectively. However, the predicted induction times lie far outside the calibration ranges specified  
469 in this study and may therefore be inaccurate. Nevertheless, since these projected APP induction times are also  
470 within the suggested residence times of treated water in the upper ocean layers, it is necessary to conduct  
471 studies lasting at least for the projected timespans, depending on the local environmental conditions.

472 Significantly shorter induction times were identified for subtropical conditions (Temp.  $\sim 23^\circ\text{C}$ , Sal.  $\sim 36$  psu, TA  
473  $\sim 2400 \mu\text{mol kg}^{-1}$ ). Hartmann et al. (2023) described an onset of the precipitation after just 4 days for a [50](#)  
474 [µm](#) filtered neq incubation with initial values of  $1050 \mu\text{mol kg}^{-1}$  for  $\Delta TA$  and  $\sim 15$  for  $\Omega_{ar}$ . Within the same  
475 setting, Paul et al. (2024) observed aragonite formation for a  $\text{CO}_2$  equilibrated setup with  $\Delta TA \sim 2300 \mu\text{mol kg}^{-1}$   
476 and  $\Omega_{ar} 9.74 \pm 0.15$  in mesocosms after 21 days.

477 The upper end members of TA perturbations presented in this study (neq:  $\Delta TA > 2400 \mu\text{mol kg}^{-1}$ ; eq:  $\Delta TA > 9000$   
478  $\mu\text{mol kg}^{-1}$ ) are not expected to represent realizable target background values for permanent open world  
479 scenarios, which would likely be aligned with biological compatibility. High perturbations would just occur within  
480 short timeframes in the near field of an injection site or within enclosed environments without sufficient  
481 potential for dilution with untreated water. The implemented gradient approach allowed to examine the  
482 principles of secondary carbonate formation under controlled conditions. While such small-scale incubations

483 provide only a limited analogue for natural systems, they nonetheless permit the investigation of fundamental  
484 processes in a well-controlled setup.

485

#### 486 **4.6 Consequence of sinking particles removing surface area for carbonate formation**

487 Because the TA-loss rate is proportional to the surface area of particles (Eq. (4)), removal of particles due to  
488 sinking processes or dilution with untreated water would result in slower precipitation rates. Small, formed  
489 particles may remain in the upper layer for several months (Fig. 8), while medium-sized particles may leave the  
490 treated water within a couple of days, depending on temperature and salinity conditions (Figs. 8 and ~~S9S7~~).  
491 Particles larger than 15  $\mu\text{m}$  are expected to sink within one day under the environmental conditions of the  
492 Raunefjorden. If those particles were removed by sinking while they were still growing, it can be estimated that  
493 approximately 30-40% of the available surface area would be removed from the upper 10 m of the water column  
494 within one day (also see SI). This would decrease the precipitation rate accordingly as surface area and formation  
495 rates are linearly proportional. In a natural open ocean environment, the formation and sinking of precipitates  
496 are likely to interact with the existing background of organic and inorganic particles. While any type of particles  
497 could potentially serve as nucleation sites,~~Potential~~ aggregation would increase the sinking speed. These  
498 processes were ~~and was~~ not ~~included~~~~considered~~ in ~~the current~~~~this~~ model ~~calculation~~~~seaculation~~ but may be  
499 relevant under different conditions~~in other settings~~. In general, the abundance and sinking of particles need to  
500 be addressed if the stability or loss of is to be assessed with a high level of confidence.

501 Efficient dilution of the treated water parcels could therefore significantly reduce ongoing precipitation,  
502 especially if the onset of the APP is initiated within the first few seconds. For example, this could be the case in  
503 the wake of a ship, in OAE applications utilizing existing marine traffic to distribute ~~TA~~alkalinity throughout the  
504 world's oceans (Caserini et al., 2021). However, particle-based alkalization approaches would nevertheless  
505 temporarily introduce additional surface area until its complete dissolution, and may cause the shift into the APP  
506 (Hartmann et al., 2023).

507 **5 Conclusion**

508 ~~TA~~Alkalinity leakage due to oversaturation sets a limit to the efficiency of OAE approaches. So far, the drivers of  
509 the process could not be quantified, preventing the implementation of TA-loss terms in applicability assessments  
510 for OAE. An induced runaway process follows predictable patterns that can be modeled using available surface  
511 area and aragonite oversaturation, identified as the main factors for the given environmental settings.  
512 However, it is expected that parameterizations will systematically change along temperature and salinity  
513 gradients, as well as with naturally occurring variations in particle abundance and quality. The determination of  
514 their impact was not within the scope of this work, instead this study aimed to provide a framework for how such  
515 needed parameterization can be achieved. Achieving a predictability of the induced TA-loss on a global scale  
516 would allow the identification of suitable locations for OAE or optimizing applications. Therefore, further  
517 research across salinity and temperature gradients would also enhance the predictive capabilities of ocean  
518 models. Runaway TA-loss processes, as described in this study, would be significantly altered under natural  
519 conditions by dilution and particle export processes. If sinking of particles and dilution with untreated water are  
520 considered, the limitations of laboratory bottle experiments become evident. Nevertheless, they contribute  
521 valuable parameterizations for model development. Field experiments are necessary to evaluate the validity of  
522 the presented theoretical model framework with respect to dilution and particle sinking processes.  
523

524 **Data availability**

525 All datasets will be made available at the time of publication.

526 **Author contributions**

527 The idea for this work was conceived by NS, with contributions by JH and SV. NS, SV and PS performed the surface  
528 area- and sinking velocity/density measurements. NS interpreted the data with help from all co-authors. NS and  
529 JH wrote the text with contributions from all co-authors.

530 **Acknowledgements**

531 Peggy Bartsch (UHH), Carl Lim (UHH) and Julieta Schneider (GEOMAR) are thanked for supporting the preparation  
532 and execution of the experiments.

533 **Financial support**

534 This research has been supported by the German Federal Ministry of Education and Research through the  
535 CDRmare projects RETAKE-1: grant no. 03F0895F and RETAKE-2: grant no. 03F0965F; Horizon 2020 (OceanNETs;  
536 grant no. 869357); the Deutsche Forschungsgemeinschaft (grant no. 390683824), under Germany's Excellence  
537 Strategy (EXC 2037, "CLICCS"; grant no. 390683824) contribution to the Center for Earth System Research and  
538 Sustainability (CEN) of ~~the University of~~ Universität Hamburg, as well as the Ocean Alk-Align project ~~Alkalinity~~  
539 Enhancement (OAE) R&D Program funded by the Carbon to Sea Initiative.

540 **Competing interests**

541 JHA is consulting the Planeteers GmbH. The contact authors have declared that all other authors have no  
542 competing interests.

543 **References**

- 544 Bach, L. T., Riebesell, U., Sett, S., Febiri, S., Rzepka, P., & Schulz, K. G. (2012). An approach for particle sinking  
545 velocity measurements in the 3–400 µm size range and considerations on the effect of temperature on  
546 sinking rates. *Marine Biology*, 159(8), 1853-1864. <https://doi.org/10.1007/s00227-012-1945-2>
- 547 Badjatya, P., Akca, A. H., Fraga Alvarez, D. V., Chang, B., Ma, S., Pang, X., Wang, E., van Hinsberg, Q., Esposito, D.  
548 V., & Kawashima, S. (2022). Carbon-negative cement manufacturing from seawater-derived magnesium  
549 feedstocks. *Proc Natl Acad Sci U S A*, 119(34), e2114680119.  
550 <https://doi.org/https://doi.org/10.1073/pnas.2114680119>
- 551 Berner, R. A. (1975). The role of magnesium in the crystal growth of calcite and aragonite from sea water.  
552 *Geochimica et Cosmochimica Acta*, 39(4), 489-504. [https://doi.org/https://doi.org/10.1016/0016-  
553 7037\(75\)90102-7](https://doi.org/https://doi.org/10.1016/0016-7037(75)90102-7)
- 554 Bialik, O. M., Sisma-Ventura, G., Vogt-Vincent, N., Silverman, J., & Katz, T. (2022). Role of oceanic abiotic  
555 carbonate precipitation in future atmospheric CO<sub>2</sub> regulation. *Sci Rep*, 12(1), 15970.  
556 <https://doi.org/https://doi.org/10.1038/s41598-022-20446-7>
- 557 Broecker, W. S., & Takahashi, T. (1966). Calcium carbonate precipitation on the Bahama Banks. *Journal of*  
558 *Geophysical Research*, 71(6), 1575-1602. <https://doi.org/https://doi.org/10.1029/JZ071i006p01575>
- 559 Brunauer, S., Emmett, P. H., & Teller, E. (1938). Adsorption of gases in multimolecular layers. *Journal of the*  
560 *American chemical society*, 60(2), 309-319.
- 561 Burton, E. A., & Walter, L. M. (1990). The role of pH in phosphate inhibition of calcite and aragonite precipitation  
562 rates in seawater. *Geochimica et Cosmochimica Acta*, 54(3), 797-808.  
563 [https://doi.org/https://doi.org/10.1016/0016-7037\(90\)90374-T](https://doi.org/https://doi.org/10.1016/0016-7037(90)90374-T)
- 564 Bustos-Serrano, H., Morse, J. W., & Millero, F. J. (2009). The formation of whittings on the Little Bahama Bank.  
565 *Marine Chemistry*, 113(1-2), 1-8. <https://doi.org/https://doi.org/10.1016/j.marchem.2008.10.006>
- 566 Caserini, S., Pagano, D., Campo, F., Abbà, A., De Marco, S., Righi, D., Renforth, P., & Grosso, M. (2021). Potential  
567 of Maritime Transport for Ocean Liming and Atmospheric CO<sub>2</sub> Removal. *Frontiers in Climate*, 3.  
568 <https://doi.org/https://doi.org/10.3389/fclim.2021.575900>
- 569 Chave, K. E., & Suess, E. (1970). Calcium Carbonate Saturation in Seawater: Effects of Dissolved Organic Matter.  
570 *Limnology and Oceanography*, 15(4), 633-637.  
571 <https://doi.org/https://doi.org/10.4319/lo.1970.15.4.0633>
- 572 Eisaman, M., Geilert, S., Renforth, P., Bastianini, L., Campbell, J., Dale, A., Foteinis, S., Grasse, P., Hawrot, O., &  
573 Löscher, C. (2023). Chapter 3: Assessing the technical aspects of OAE approaches. *State of the Planet*  
574 *Discussions*, 2023, 1-52. <https://doi.org/https://doi.org/10.5194/sp-2-0ae2023-3-2023>
- 575 Faucher, G., Haunost, M., Paul, A. J., Tietz, A. U. C., & Riebesell, U. (2024). Growth response of *Emiliania huxleyi*  
576 to ocean alkalinity enhancement. *EGU sphere*, 2024, 1-17. [https://doi.org/10.5194/egusphere-2024-  
577 2201](https://doi.org/10.5194/egusphere-2024-2201)
- 578 Ferderer, A., Chase, Z., Kennedy, F., Schulz, K. G., & Bach, L. T. (2022). Assessing the influence of ocean alkalinity  
579 enhancement on a coastal phytoplankton community. *Biogeosciences*, 19(23), 5375-5399.  
580 <https://doi.org/10.5194/bg-19-5375-2022>
- 581 Fuhr, M., Geilert, S., Schmidt, M., Liebetrau, V., Vogt, C., Ledwig, B., & Wallmann, K. (2022). Kinetics of Olivine  
582 Weathering in Seawater: An Experimental Study. *Frontiers in Climate*, 4.  
583 <https://doi.org/https://doi.org/10.3389/fclim.2022.831587>
- 584 Fuss, S., Lamb, W. F., Callaghan, M. W., Hilaire, J., Creutzig, F., Amann, T., Beringer, T., de Oliveira Garcia, W.,  
585 Hartmann, J., Khanna, T., Luderer, G., Nemet, G. F., Rogelj, J., Smith, P., Vicente, J. L. V., Wilcox, J., del  
586 Mar Zamora Dominguez, M., & Minx, J. C. (2018). Negative emissions—Part 2: Costs, potentials and side  
587 effects. *Environmental Research Letters*, 13(6). <https://doi.org/10.1088/1748-9326/aabf9f>
- 588 Gately, J. A., Kim, S. M., Jin, B., Brzezinski, M. A., & Iglesias-Rodriguez, M. D. (2023). Coccolithophores and diatoms  
589 resilient to ocean alkalinity enhancement: A glimpse of hope? *Science Advances*, 9(24), eadg6066.  
590 <https://doi.org/10.1126/sciadv.adg6066>
- 591 Goldenberg, S. U., Riebesell, U., Brüggemann, D., Börner, G., Sswat, M., Folkvord, A., Couret, M., Spjelkavik, S.,  
592 Sánchez, N., Jaspers, C., & Moyano, M. (2024). Early life stages of fish under ocean alkalinity  
593 enhancement in coastal plankton communities. *Biogeosciences*, 21(20), 4521-4532.  
594 <https://doi.org/10.5194/bg-21-4521-2024>
- 595 Haas, A. R. (1916). The Effect of the Addition of Alkali to Sea Water Upon the Hydrogen Ion Concentration. *Journal*  
596 *of Biological Chemistry*, 26(2), 515-517. [https://doi.org/https://doi.org/10.1016/s0021-9258\(18\)87433-  
597 6](https://doi.org/https://doi.org/10.1016/s0021-9258(18)87433-6)

598 Hartmann, J., Suitner, N., Lim, C., Schneider, J., Marín-Samper, L., Arístegui, J., Renforth, P., Taucher, J., &  
599 Riebesell, U. (2023). Stability of alkalinity in ocean alkalinity enhancement (OAE) approaches –  
600 consequences for durability of CO<sub>2</sub> storage. *Biogeosciences*, 20(4), 781-802.  
601 <https://doi.org/https://doi.org/10.5194/bg-20-781-2023>

602 Hartmann, J., West, A. J., Renforth, P., Köhler, P., De La Rocha, C. L., Wolf-Gladrow, D. A., Dürr, H. H., & Scheffran,  
603 J. (2013). Enhanced chemical weathering as a geoengineering strategy to reduce atmospheric carbon  
604 dioxide, supply nutrients, and mitigate ocean acidification. *Reviews of Geophysics*, 51(2), 113-149.  
605 <https://doi.org/https://doi.org/10.1002/rog.20004>

606 Harvey, L. D. D. (2008). Mitigating the atmospheric CO<sub>2</sub> increase and ocean acidification by adding limestone  
607 powder to upwelling regions. *Journal of Geophysical Research: Oceans*, 113(C4).  
608 <https://doi.org/10.1029/2007jc004373>

609 He, J., & Tyka, M. D. (2023). Limits and CO<sub>2</sub> equilibration of near-coast alkalinity enhancement. *Biogeosciences*,  
610 20(1), 27-43. <https://doi.org/https://doi.org/10.5194/bg-20-27-2023>

611 Ilyina, T., Six, K. D., Segschneider, J., Maier-Reimer, E., Li, H., & Núñez-Riboni, I. (2013). Global ocean  
612 biogeochemistry model HAMOCC: Model architecture and performance as component of the MPI-Earth  
613 system model in different CMIP5 experimental realizations. *Journal of Advances in Modeling Earth  
614 Systems*, 5(2), 287–315. <https://doi.org/https://doi.org/10.1029/2012ms000178>

615 Inskeep, W. P., & Bloom, P. R. (1985). An evaluation of rate equations for calcite precipitation kinetics at pCO<sub>2</sub>  
616 less than 0.01 atm and pH greater than 8. *Geochimica et Cosmochimica Acta*, 49(10), 2165-2180.  
617 [https://doi.org/https://doi.org/10.1016/0016-7037\(85\)90074-2](https://doi.org/https://doi.org/10.1016/0016-7037(85)90074-2)

618 IPCC. (2023). Technical Summary. In *Climate Change 2021 – The Physical Science Basis* (pp. 35-144).  
619 <https://doi.org/10.1017/9781009157896.002>

620 Iyer, G., Hultman, N., Eom, J., McJeon, H., Patel, P., & Clarke, L. (2015). Diffusion of low-carbon technologies and  
621 the feasibility of long-term climate targets. *Technological Forecasting and Social Change*, 90, 103-118.  
622 <https://doi.org/10.1016/j.techfore.2013.08.025>

623 Kapp, E. M. (1928). The precipitation of calcium and magnesium from sea water by sodium hydroxide. *The  
624 Biological Bulletin*, 55(6), 453-458.

625 Kellock, C., Castillo Alvarez, M. C., Finch, A., Penkman, K., Kroger, R., Clog, M., & Allison, N. (2022). Optimising a  
626 method for aragonite precipitation in simulated biogenic calcification media. *PLoS One*, 17(12),  
627 e0278627. <https://doi.org/https://doi.org/10.1371/journal.pone.0278627>

628 Khesghi, H. S. (1995). Sequestering atmospheric carbon dioxide by increasing ocean alkalinity. *Energy*, 20(9), 915-  
629 922. [https://doi.org/https://doi.org/10.1016/0360-5442\(95\)00035-F](https://doi.org/https://doi.org/10.1016/0360-5442(95)00035-F)

630 Marín-Samper, L., Arístegui, J., Hernández-Hernández, N., Ortiz, J., Archer, S. D., Ludwig, A., & Riebesell, U.  
631 (2024). Assessing the impact of CO<sub>2</sub>-equilibrated ocean alkalinity enhancement on microbial metabolic  
632 rates in an oligotrophic system. *Biogeosciences*, 21(11), 2859-2876. [https://doi.org/10.5194/bg-21-  
633 2859-2024](https://doi.org/10.5194/bg-21-2859-2024)

634 Marion, G., Millero, F., & Feistel, R. (2009). Precipitation of solid phase calcium carbonates and their effect on  
635 application of seawater S A–T–P models. *Ocean science*, 5(3), 285-291.  
636 <https://doi.org/https://doi.org/10.5194/os-5-285-2009>

637 Minx, J. C., Lamb, W. F., Callaghan, M. W., Fuss, S., Hilaire, J., Creutzig, F., Amann, T., Beringer, T., de Oliveira  
638 Garcia, W., Hartmann, J., Khanna, T., Lenzi, D., Luderer, G., Nemet, G. F., Rogelj, J., Smith, P., Vicente  
639 Vicente, J. L., Wilcox, J., & del Mar Zamora Dominguez, M. (2018). Negative emissions—Part 1: Research  
640 landscape and synthesis. *Environmental Research Letters*, 13(6). [https://doi.org/10.1088/1748-  
641 9326/aabf9b](https://doi.org/10.1088/1748-9326/aabf9b)

642 Moras, C. A., Bach, L. T., Cyronak, T., Joannes-Boyau, R., & Schulz, K. G. (2022). Ocean alkalinity enhancement –  
643 avoiding runaway CaCO<sub>3</sub> precipitation during quick and hydrated lime dissolution. *Biogeosciences*,  
644 19(15), 3537-3557. <https://doi.org/https://doi.org/10.5194/bg-19-3537-2022>

645 Moras, C. A., Cyronak, T., Bach, L. T., Joannes-Boyau, R., & Schulz, K. G. (2024). Effects of grain size and seawater  
646 salinity on magnesium hydroxide dissolution and secondary calcium carbonate precipitation kinetics:  
647 implications for ocean alkalinity enhancement. *Biogeosciences*, 21(14), 3463-3475.  
648 <https://doi.org/10.5194/bg-21-3463-2024>

649 Morse, J. W., Arvidson, R. S., & Lüttge, A. (2007). Calcium carbonate formation and dissolution. *Chemical reviews*,  
650 107(2), 342-381. <https://doi.org/https://doi.org/10.1021/cr050358j>

651 Morse, J. W., Gledhill, D. K., & Millero, F. J. (2003). CaCO<sub>3</sub> precipitation kinetics in waters from the great Bahama  
652 bank. *Geochimica et Cosmochimica Acta*, 67(15), 2819-2826.  
653 [https://doi.org/https://doi.org/10.1016/s0016-7037\(03\)00103-0](https://doi.org/https://doi.org/10.1016/s0016-7037(03)00103-0)

654 Morse, J. W., & He, S. (1993). Influences of T, S and PCO<sub>2</sub> on the pseudo-homogeneous precipitation of CaCO<sub>3</sub>  
655 from seawater: implications for whiting formation. *Marine Chemistry*, 41(4), 291-297.  
656 [https://doi.org/https://doi.org/10.1016/0304-4203\(93\)90261-L](https://doi.org/https://doi.org/10.1016/0304-4203(93)90261-L)

657 Mucci, A., & Morse, J. W. (1983). The incorporation of Mg<sup>2+</sup> and Sr<sup>2+</sup> into calcite overgrowths: influences of  
658 growth rate and solution composition. *Geochimica et Cosmochimica Acta*, 47(2), 217-233.  
659 [https://doi.org/https://doi.org/10.1016/0016-7037\(83\)90135-7](https://doi.org/https://doi.org/10.1016/0016-7037(83)90135-7)

660 Oschlies, A., Bach, L. T., Rickaby, R. E. M., Satterfield, T., Webb, R., & Gattuso, J.-P. (2023). Climate targets, carbon  
661 dioxide removal, and the potential role of ocean alkalinity enhancement. *State of the Planet, 2-oae2023*,  
662 1-9. <https://doi.org/10.5194/sp-2-oae2023-1-2023>

663 Ou, Y., Xue, Z. G., & Hu, X. (2025). A numerical assessment of ocean alkalinity enhancement efficiency on a river-  
664 dominated continental shelf – a case study in the northern Gulf of Mexico. *Environmental Research*  
665 *Letters*. <https://doi.org/10.1088/1748-9326/adaa8b>

666 Pan, Y., Li, Y., Ma, Q., He, H., Wang, S., Sun, Z., Cai, W.-J., Dong, B., Di, Y., Fu, W., & Chen, C.-T. A. (2021). The role  
667 of Mg<sup>2+</sup> in inhibiting CaCO<sub>3</sub> precipitation from seawater. *Marine Chemistry*, 237.  
668 <https://doi.org/https://doi.org/10.1016/j.marchem.2021.104036>

669 Paul, A. J., Haunost, M., Goldenberg, S. U., Hartmann, J., Sanchez, N. S., Schneider, J., Suitner, N., & Riebesell, U.  
670 (2024). Ocean alkalinity enhancement in an open ocean ecosystem: Biogeochemical responses and  
671 carbon storage durability. *EGUsphere*. <https://doi.org/https://doi.org/10.5194/egusphere-2024-417>

672 Pokrovsky, O. S. (1998). Precipitation of calcium and magnesium carbonates from homogeneous supersaturated  
673 solutions. *Journal of Crystal Growth*, 186(1-2), 233-239. [https://doi.org/https://doi.org/10.1016/S0022-](https://doi.org/https://doi.org/10.1016/S0022-0248(97)00462-4)  
674 [0248\(97\)00462-4](https://doi.org/https://doi.org/10.1016/S0022-0248(97)00462-4)

675 Pytkowicz, R. (1973). Calcium carbonate retention in supersaturated seawater. *American Journal of Science*,  
676 273(6), 515-522. <https://doi.org/http://dx.doi.org/10.2475/ajs.273.6.515>

677 Pytkowicz, R. M. (1965). Rates of Inorganic Calcium Carbonate Nucleation. *The Journal of Geology*, 73(1), 196-  
678 199. <https://doi.org/10.1086/627056>

679 Ramírez, L., Pozzo-Pirotta, L. J., Trebec, A., Manzanares-Vázquez, V., Díez, J. L., Arístegui, J., Riebesell, U., Archer,  
680 S. D., & Segovia, M. (2024). Ocean Alkalinity Enhancement (OAE) does not cause cellular stress in a  
681 phytoplankton community of the sub-tropical Atlantic Ocean. *EGUsphere*, 2024, 1-34.  
682 <https://doi.org/https://doi.org/10.5194/egusphere-2024-847>

683 Rau, G. H., & Caldeira, K. (1999). Enhanced carbonate dissolution as a means of sequestering carbon dioxide in  
684 the ocean. *Energy Conversion and Management*, 40(17), 1803-1813. [https://doi.org/10.1016/S0196-](https://doi.org/10.1016/S0196-8904(99)00071-0)  
685 [8904\(99\)00071-0](https://doi.org/10.1016/S0196-8904(99)00071-0)

686 Renforth, P., & Henderson, G. (2017). Assessing ocean alkalinity for carbon sequestration. *Reviews of Geophysics*,  
687 55(3), 636-674. <https://doi.org/https://doi.org/10.1002/2016rg000533>

688 Ringham, M. C., Hirtle, N., Shaw, C., Lu, X., Herndon, J., Carter, B. R., & Eisaman, M. D. (2024). An assessment of  
689 ocean alkalinity enhancement using aqueous hydroxides: kinetics, efficiency, and precipitation  
690 thresholds. *Biogeosciences*, 21(15), 3551-3570. [https://doi.org/https://doi.org/10.5194/bg-21-3551-](https://doi.org/https://doi.org/10.5194/bg-21-3551-2024)  
691 [2024](https://doi.org/https://doi.org/10.5194/bg-21-3551-2024)

692 Rogelj, J., Popp, A., Calvin, K. V., Luderer, G., Emmerling, J., Gernaat, D., Fujimori, S., Strefler, J., Hasegawa, T.,  
693 Marangoni, G., Krey, V., Kriegler, E., Riahi, K., van Vuuren, D. P., Doelman, J., Drouet, L., Edmonds, J.,  
694 Fricko, O., Harmsen, M.,...Tavoni, M. (2018). Scenarios towards limiting global mean temperature  
695 increase below 1.5 °C. *Nature Climate Change*, 8(4), 325-332. [https://doi.org/10.1038/s41558-018-](https://doi.org/10.1038/s41558-018-0091-3)  
696 [0091-3](https://doi.org/10.1038/s41558-018-0091-3)

697 Sánchez, N., Goldenberg, S. U., Brüggemann, D., Jaspers, C., Taucher, J., & Riebesell, U. (2024). Plankton food  
698 web structure and productivity under ocean alkalinity enhancement. *Science Advances*, 10(49),  
699 eado0264. <https://doi.org/doi:10.1126/sciadv.ado0264>

700 Schulz, K. G., Bach, L. T., & Dickson, A. G. (2023). Seawater carbonate chemistry considerations for ocean  
701 alkalinity enhancement research: theory, measurements, and calculations. *Guide to Best Practices in*  
702 *Ocean Alkalinity Enhancement Research, 2-oae2023*, 2. <https://doi.org/10.5194/sp-2-oae2023-2-2023>

703 Schwinger, J., Bourgeois, T., & Rickels, W. (2024). On the emission-path dependency of the efficiency of ocean  
704 alkalinity enhancement. *Environmental Research Letters*, 19(7). [https://doi.org/10.1088/1748-](https://doi.org/10.1088/1748-9326/ad5a27)  
705 [9326/ad5a27](https://doi.org/10.1088/1748-9326/ad5a27)

706 Sers, M. R., & Victor, P. A. (2018). The Energy-emissions Trap. *Ecological Economics*, 151, 10-21.  
707 <https://doi.org/10.1016/j.ecolecon.2018.04.004>

708 Sjöberg, E. (1976). A fundamental equation for calcite dissolution kinetics. *Geochimica et Cosmochimica Acta*,  
709 40(4), 441-447. [https://doi.org/https://doi.org/10.1016/0016-7037\(76\)90009-0](https://doi.org/https://doi.org/10.1016/0016-7037(76)90009-0)

710 Söhnel, O., & Mullin, J. W. (1988). Interpretation of crystallization induction periods. *Journal of colloid and*  
711 *interface science*, 123(1), 43-50. [https://doi.org/https://doi.org/10.1016/0021-9797\(88\)90219-6](https://doi.org/https://doi.org/10.1016/0021-9797(88)90219-6)

712 Suessle, P., Taucher, J., Goldenberg, S., Baumann, M., Spilling, K., Noche-Ferreira, A., Vanharanta, M., & Riebesell,  
713 U. (2023). Particle fluxes by subtropical pelagic communities under ocean alkalinity enhancement.  
714 *EGUsphere*, 2023, 1-26. <https://doi.org/https://doi.org/10.5194/egusphere-2023-2800>  
715 Suitner, N., Faucher, G., Lim, C., Schneider, J., Moras, C. A., Riebesell, U., & Hartmann, J. (2024). Ocean alkalinity  
716 enhancement approaches and the predictability of runaway precipitation processes: results of an  
717 experimental study to determine critical alkalinity ranges for safe and sustainable application scenarios.  
718 *Biogeosciences*, 21(20), 4587-4604. <https://doi.org/10.5194/bg-21-4587-2024>  
719 Tjørve, K. M., & Tjørve, E. (2017). The use of Gompertz models in growth analyses, and new Gompertz-model  
720 approach: An addition to the Unified-Richards family. *PLoS One*, 12(6), e0178691.  
721 <https://doi.org/https://doi.org/10.1371/journal.pone.0178691>  
722 UNFCCC. (2015). Report of the Conference of the Parties to the United Nations Framework Convention on  
723 Climate Change (21st Session, 2015: Paris). Retrived December. Vol. 4. 2015.  
724 Varliero, S., Buono, A., Caserini, S., Raos, G., & Macchi, P. (2024). Chemical Aspect of Ocean Liming for CO2  
725 Removal: Dissolution Kinetics of Calcium Hydroxide in Seawater. *ACS Engineering Au*.  
726 <https://doi.org/https://doi.org/10.1021/acsengineeringau.4c00008>  
727 Wang, H., Pilcher, D. J., Kearney, K. A., Cross, J. N., Shugart, O. M., Eisaman, M. D., & Carter, B. R. (2023). Simulated  
728 impact of ocean alkalinity enhancement on atmospheric CO2 removal in the Bering Sea. *Earth's Future*,  
729 11(1). [https://doi.org/ https://doi.org/10.1029/2022EF002816](https://doi.org/https://doi.org/10.1029/2022EF002816)  
730 Wells, M. L., & Goldberg, E. D. (1992). Marine submicron particles. *Marine Chemistry*, 40(1-2), 5-18.  
731 [https://doi.org/https://doi.org/10.1016/0304-4203\(92\)90045-C](https://doi.org/https://doi.org/10.1016/0304-4203(92)90045-C)  
732 Wurgaft, E., Steiner, Z., Luz, B., & Lazar, B. (2016). Evidence for inorganic precipitation of CaCO3 on suspended  
733 solids in the open water of the Red Sea. *Marine Chemistry*, 186, 145-155.  
734 <https://doi.org/https://doi.org/10.1016/j.marchem.2016.09.006>  
735 Wurgaft, E., Wang, Z. A., Churchill, J. H., Dellapenna, T., Song, S., Du, J., Ringham, M. C., Rivlin, T., & Lazar, B.  
736 (2021). Particle Triggered Reactions as an Important Mechanism of Alkalinity and Inorganic Carbon  
737 Removal in River Plumes. *Geophysical Research Letters*, 48(11), 277.  
738 <https://doi.org/https://doi.org/10.1029/2021gl093178>  
739 Xin, X., Goldenberg, S. U., Taucher, J., Stühr, A., Aristegui, J., & Riebesell, U. (2024). Resilience of Phytoplankton  
740 and Microzooplankton Communities under Ocean Alkalinity Enhancement in the Oligotrophic Ocean.  
741 *Environ Sci Technol*. <https://doi.org/10.1021/acs.est.4c09838>  
742 Zeebe, R., & Wolf-Gladrow, D. (2001). *CO2 in Seawater: Equilibrium, Kinetics, Isotopes*. Elsevier Oceanography  
743 Book Series. 65.  
744 Zhong, S., & Mucci, A. (1989). Calcite and aragonite precipitation from seawater solutions of various salinities:  
745 Precipitation rates and overgrowth compositions. *Chemical geology*, 78(3-4), 283-299.  
746 [https://doi.org/https://doi.org/10.1016/0009-2541\(89\)90064-8](https://doi.org/https://doi.org/10.1016/0009-2541(89)90064-8)  
747 Zhou, M., Tyka, M. D., Ho, D. T., Yankovsky, E., Bachman, S., Nicholas, T., Karspeck, A. R., & Long, M. C. (2024).  
748 Mapping the global variation in the efficiency of ocean alkalinity enhancement for carbon dioxide  
749 removal. *Nature Climate Change*, 1-7. <https://doi.org/https://doi.org/10.1038/s41558-024-02179-9>

750